This is a preprint, the final version is subject to change, of the American Mineralogist (MSA)
Cite as Authors (Year) Title. American Mineralogist, in press.
DOI: https://doi.org/10.2138/am-2019-7036

(Revision 2)

Controls on tetrahedral Fe(III) abundance in 2:1 phyllosilicates

Javier Cuadros[a], Joseph R. Michalski[a,b], M. Darby Dyar[c], Vesselin Dekov[d]

[a] Department of Earth Sciences, Natural History Museum, Cromwell Road, London SW7 5BD, UK (j.cuadros@nhm.ac.uk)

[b] Department of Earth Sciences and Laboratory for Space Research, University of Hong Kong, Hong Kong, China (jmichal@hku.hk)

[c] Department of Astronomy, Mount Holyoke College, South Hadley, MA, 01075 USA (mdyar@mtholyoke.edu)

[d] Department of Ocean Sciences, Tokyo University of Marine Science and Technology, 4-5-7 Konan, Minato-ku, Tokyo 108-8477, Japan; e-mail (vdekov0@kaiyodai.ac.jp)

Short title: Controls on tetrahedral Fe(III) in 2:1 phyllosilicates

Corresponding author: Javier Cuadros; j.cuadros@nhm.ac.uk

This is a preprint, the final version is subject to change, of the American Mineralogist (MSA)
Cite as Authors (Year) Title. American Mineralogist, in press.
DOI: https://doi.org/10.2138/am-2019-7036

ABSTRACT

Iron (II) only occupies octahedral sites in phyllosilicates, whereas Fe(III) can occupy both octahedral and tetrahedral sites. The controls on Fe(III) distribution between tetrahedral and octahedral sites have been a matter of great interest in order to understand the interplay between formation environment (Fe abundance, redox conditions) and crystal-chemical factors (stability of the crystal lattice) during crystallization of Fe-phyllosilicates. Here, for the first time, we present a model of Fe(III) distribution in 2:1 phyllosilicates. We investigated 21 samples of 2:1 phyllosilicates of submarine hydrothermal origin using XRD, chemical analysis and Mössbauer spectroscopy (and other supporting techniques not presented here). An additional dataset of 49 analyses of 2:1 phyllosilicates from the literature was also used. Overall, the data cover a wide range of dioctahedral and trioctahedral phyllosilicates, including endmember minerals and interstratified phases. Dioctahedral phyllosilicates have a steric control whereby tetrahedral Fe(III) is only allowed if at least five out of six octahedral atoms are larger than Al (typically Fe[III], Fe[II], Mg) that produces an expanded structure where tetrahedral sites can accommodate Fe(III). After this threshold, further Fe(III) atoms occupy tetrahedral sites preferentially (~73 % of further Fe[III] atoms) over octahedral sites. In trioctahedral 2:1 phyllosilicates there is no steric hindrance to tetrahedral Fe(III) because the crystal dimensions are such that tetrahedral sites can accommodate Fe(III). On average, Fe(III) enters tetrahedral and octahedral sites in similar proportion, and the only apparent control on tetrahedral Fe(III) abundance is Fe(III) availability during crystallization. This model allows to predict Fe(III) distribution between structural sites, provides an avenue for further exploration of the thermodynamic stability of phyllosilicates using cationic size, and provides a tool to better describe stability/reactivity of Fe-rich phyllosilicates, the most reactive of phyllosilicates and very relevant in geochemical and biological processes.

Keywords: Dioctahedral 2:1 phyllosilicates; Fe; Tetrahedral Fe; Trioctahedral 2:1 phyllosilicates.

This is a preprint, the final version is subject to change, of the American Mineralogist (MSA)
Cite as Authors (Year) Title. American Mineralogist, in press.
DOI: https://doi.org/10.2138/am-2019-7036

INTRODUCTION

Iron-rich phyllosilicates are important because they are more reactive than their Al- and Mg-rich counterparts. Phyllosilicates with significant Fe(II) content, typically trioctahedral, are weathered more rapidly than Al- and Mg-rich ones (Wilson 2004). Iron in phyllosilicates may undergo oxidation and reduction, which has immediate effect on mineral stability, due to modifications to the layer charge. Typically, Fe oxidation state in non-expanding phyllosilicates is not affected by inorganic agents, unless they are extreme (e.g., hydrothermal fluids, strong acid attack). However, microorganisms can modify Fe oxidation state to a certain extent in non-expandable phyllosilicates (e.g., illite, chlorite; Dong et al. 2009). In expandable phyllosilicates (smectite, vermiculite), Fe oxidation state is influenced by both external redox conditions (Fialips et al. 2002) and the direct action of microorganisms (Jaisi et al. 2005). The above reactions are important for microorganism respiration and, more generally, in soils, where water saturation conditions, microbial activity, and organic matter concentration change Fe oxidation state in phyllosilicates. As a consequence, these minerals may experience changes of particle size, particle aggregation state, cation exchange capacity, and even their mineralogy (Stucki et al. 2002; Cuadros 2017). Such changes influence further bio-geochemical processes. Recent articles have demonstrated that Fe in environments with redox fluctuations causes rapid formation of Fe-illite or glauconite from kaolinite or smectite, in reactions of geochemical significance at a global scale (Baldermann et al. 2015; Cuadros et al. 2017). As a consequence of all the above, Fe in phyllosilicates promotes faster mineralogical and chemical changes, and a greater, more intense interaction of these minerals with their biological and inorganic environment. Improved understanding of the crystal-chemistry of Fe-phyllosilicates will help to better establish their reactivity.

Iron most frequently occupies octahedral sites in phyllosilicates. In a first evaluation, it appears that both Fe(II) and Fe(III) fit better within the larger octahedral site than in the smaller tetrahedral site. Iron (III) occupies tetrahedral sites but no Fe(II) has been found so far occupying tetrahedral sites in

This is a preprint, the final version is subject to change, of the American Mineralogist (MSA)
Cite as Authors (Year) Title. American Mineralogist, in press.
DOI: https://doi.org/10.2138/am-2019-7036

phyllosilicates or, more generally, in silicates. In phyllosilicates, Fe(II) does not enter tetrahedral sites probably due to the combination of large ionic radius (0.71 Å in a tetrahedral environment according to Whittaker and Muntus 1970; compare with the tetrahedral ionic radii of Si and Al of 0.26 and 0.39 Å, respectively, from Shannon 1976) and divalent electric charge that does not balance efficiently the negative charge of oxide anions in corner-shared tetrahedra. Iron (III), however, with a trivalent charge and smaller radius (tetrahedral ionic radius of 0.57 Å; Whittaker and Muntus 1970) mitigates totally or partially these hindrances. The distribution of Fe(III) between the tetrahedral and octahedral sheets in phyllosilicates is generally displaced towards the octahedra. It has been frequently assumed that phyllosilicates with low to medium Fe(III) content have no tetrahedral Fe, and thus Fe(III) presence in the tetrahedral sheet is considered only in Fe(III)-rich phyllosilicates. Even in Fe(III)-rich phyllosilicates, if no spectroscopic data were available to establish Fe(III) site location, it was frequently assumed that Fe(III) only enters the tetrahedral sheet if there is not enough Si + Al to occupy it entirely (see Gates et al. 2002, who explained this state of affairs and challenged it). Early studies (1960s and 1970s) reported evidence from Mössbauer spectroscopy that this was not necessarily the case. However, reports of tetrahedral Fe(III) in phyllosilicates have been controversial due to lack of consensus over proper assignment of Mössbauer peaks to structural sites, as discussed below.

Detection of tetrahedral Fe(III) by Mössbauer faces several obstacles. Because tetrahedral Fe contents are frequently low, the uncertainty associated with the correspondingly low-intensity peaks in the Mössbauer spectra may be high. Further, there is overlap between the low-energy lines (low-velocity values) of tetrahedral Fe(III), octahedral Fe(III) and octahedral Fe(II) (e.g., Coey et al. 1984; Rancourt et al. 1992), making it difficult to identify tetrahedral Fe(III) and quantify it. Even if peak positions and relative intensities were correctly identified, their assignment to specific sites is controversial due to the variable range of both isomer shift and quadrupole splitting that Fe(III) displays in tetrahedral and octahedral coordination. Within individual specimens, octahedral Fe(III)

This is a preprint, the final version is subject to change, of the American Mineralogist (MSA)
Cite as Authors (Year) Title. American Mineralogist, in press.
DOI: https://doi.org/10.2138/am-2019-7036

typically displays two doublets, and possibly three (Drits et al. 1997), generated by different chemical and structural arrangements. Two octahedral Fe(II) peaks are also frequent. Initially, it was suggested that the two octahedral Fe(III) and Fe(II) sites represented cis- and trans-positions (Rozenson and Heller-Kalai 1977), and so were they assigned by several authors. Later studies, however, indicated that cis and trans octahedral sites cannot be resolved either for Fe(III) or Fe(II) (Murad and Wagner 1994; Rancourt 1994; Dyar 2002). As a result of all the above, some peak assignments to tetrahedral Fe(III) have been controversial. For example, the peak assignments to tetrahedral Fe(III) in biotite by Dyar (1990) were contested by Rancourt et al. (1992), and after further discussion and investigation were finally considered most probably caused by Fe(III) in very distorted octahedral sites (Dyar 2002). Similarly, different interpretations of Mössbauer spectra of dioctahedral 2:1 phyllosilicates have led to contrasting tetrahedral Fe(III) contents, more obviously so for low contents (Cardile 1989 and references therein).

With time, accumulated experience has helped to clarify these issues and provided increasing confidence that Mössbauer spectroscopy can reliably indicate the existence and proportion of Fe(III) in tetrahedral sites (Dyar 2002). There is now evidence that Fe(III) occupies tetrahedral sites even if Si + Al could occupy them entirely. Examples with strong evidence have used combined XANES, EXAFS, near-IR, X-ray diffraction and chemical data on nontronite (Manceau et al. 2000; Gates et al. 2002). Other studies came to the same conclusion using more indirect results, such as infrared investigation of octahedral cations in celadonites and glauconites (Slonimskaya et al. 1986; Besson and Drits 1997; Petit et al. 2015).

Accordingly, there is no doubt that Fe(III) can occupy tetrahedral sites in phyllosilicates "displacing" Al to the octahedral sheet. The question arises: what controls Fe(III) occupancy of tetrahedral sites? The extensive study by Gates et al. (2002) concluded that tetrahedral Fe is unlikely in nontronite for Fe_2O_3 <34 wt%. Previously, Dyar (1987) suggested a relation between the

This is a preprint, the final version is subject to change, of the American Mineralogist (MSA)
Cite as Authors (Year) Title. American Mineralogist, in press.
DOI: https://doi.org/10.2138/am-2019-7036

128 average size of the octahedral cations in trioctahedral micas and tetrahedral Fe occupancy. Baron et
129 al. (2016) linked formation pH with tetrahedral Fe(III) for the particular case of synthetic Si-Fe
130 nontronites. Until now, however, there is no consistent model of tetrahedral Fe(III) occupancy in
131 phyllosilicates. This unresolved question has barred progress towards deeper understanding of
132 stability and reactivity of Fe-phyllosilicates.
133
134 The first glimpse of such a model was provided by Sánchez-Marañón et al. (2018), who showed
135 that there is a threshold of Fe content in 2:1 phyllosilicates for the occurrence of tetrahedral Fe(III)
136 (Fig. 1). This threshold increases from trioctahedral phyllosilicates (approximately zero) to
137 interstratified dioctahedral-trioctahedral structures and to dioctahedral phyllosilicates (Fig. 1). The
138 samples showing this behavior are mostly originated in submarine hydrothermal sites, where Fe is
139 frequently abundant, from hydrothermal fluids and Fe sulfides (Hekinian et al. 1993); a few other
140 samples are of terrestrial origin. They were all described and investigated in detail by Cuadros et al.
141 (1993) using chemical, mineralogical, spectroscopic, and thermogravimetric methods. Further
142 spectroscopic information about the samples was provided in the near- and mid-infrared (Michalski
143 et al. 2015; Cuadros et al. 2016) and in the visible part of the spectrum (Sánchez-Marañón et al.
144 2018). In this contribution, tetrahedral Fe(III) occupancy in 2:1 phyllosilicates is further analyzed
145 using the set of samples from Cuadros et al. (2013) and 49 analyses from the literature. A model is
146 proposed describing how tetrahedral occupancy by Fe(III) takes place in both dioctahedral and
147 trioctahedral 2:1 phyllosilicates.
148
149 ## MATERIALS AND METHODS

150 ### Experimental work

151 The samples from Cuadros et al. (2013) originated mostly from several seafloor hydrothermal fields
152 with a few ones of terrestrial origin. In the present study, only those investigated with Mössbauer
153 spectroscopy are used. They are all from submarine hydrothermal sites only, and they originated

This is a preprint, the final version is subject to change, of the American Mineralogist (MSA)
Cite as Authors (Year) Title. American Mineralogist, in press.
DOI: https://doi.org/10.2138/am-2019-7036

154 from the following sites: Atlantis II Deep (Red Sea), Guaymas Basin (Gulf of California), East
155 Pacific Rise, and Mid-Atlantic Ridge.
156

157 The samples were investigated with multiple analytical techniques (Cuadros et al. 2013). The
158 techniques described here are those for which results are reported. First, the samples were
159 investigated as powders for their full mineralogy. The same powders were studied to analyze in
160 detail the 060 system (59-64 °2θ) with a PANalytical X'Pert Pro diffractometer, at 45 kV and 40
161 mA, using Cu Kα radiation, with divergence slit of 0.25°, and Soller 1 and 2 slits of 1.146°. This
162 apparatus uses a solid-state detector (X'Celerator) covering an angle of 2.1° that integrates the
163 diffracted intensity over that angle dynamically as it scans. The samples were side-loaded to avoid
164 preferential orientation of the particles. The specimens were scanned in the 59-64 °2θ range at low
165 speed (62 min scan, equivalent speed of 12.4 s/step), with a resolution of 0.0167 °2θ (scan step in a
166 conventional scanner).
167

168 Salts were then removed by dissolution in deionized water and Fe oxides by the dithionite-citrate-
169 bicarbonate method (this latter method was used only in six samples; Cuadros et al. 2013). Then,
170 the phyllosilicates were separated in the <2 μm size fraction by dispersion in deionized water and
171 centrifugation. For the detailed description of such methods and the specific mineral phases
172 removed see Cuadros et al. (2013) and the corresponding supplementary information. All results
173 reported here except those of the XRD 060 peak system correspond to the <2 μm size fraction. X-
174 ray diffraction of oriented mounts was used to identify the phyllosilicates, most of them consisting
175 of interstratified phases, and to quantify their respective proportions. In some cases, this study
176 revealed trace amounts of non-phyllosilicate minerals. The samples were prepared as oriented
177 mounts (10 mg of the powders dispersed in 2 ml of deionized water; pipetting of the dispersion on
178 glass slides; letting them dry). They were studied as air-dried and as intercalated with ethylene-
179 glycol (EG) (overnight in an EG-saturated atmosphere at 60 °C). The samples were investigated in

This is a preprint, the final version is subject to change, of the American Mineralogist (MSA)
Cite as Authors (Year) Title. American Mineralogist, in press.
DOI: https://doi.org/10.2138/am-2019-7036

the apparatus and conditions indicated above except that the scanning range was 2-40 °2θ and the scanning time 63 min (equivalent to 1.66 s/step). The quantification of the interstratified clay phases was carried out by modeling the patterns of EG-intercalated samples using CLAYSim from MDI. This software allows modeling of the 00l peaks of interstratified minerals with two layer components, and mixtures of up to ten such phases.

The specimens were studied with Mössbauer spectroscopy at Mount Holyoke College, Massachusetts (Cuadros et al. 2013). Sample mounts were prepared by gently mixing 30-40 mg of powdered sample with sugar in order to reduce preferred orientation. To mitigate the effects of thickness, all samples were run at <2 mg Fe/cm^2, an order of magnitude below the "ideal" thicknesses calculated by Long et al. (1983); discussion of this effect is given in Dyar et al. (2008). The mixtures were placed in a sample holder confined by Kapton tape. Mössbauer spectra were acquired at 295 K using a source of ~40 mCi ^{57}Co in Rh on a WEB Research Co. model WT302 spectrometer. For each sample, the fraction of the baseline due to the Compton scattering of 122 keV gammas by electrons inside the detector was determined by measuring the count rate with and without a 14.4-keV stop filter (~2 mm of Al foil) in the gamma beam. Compton-corrected absorption was calculated for each spectrum with the formula $A/(1 - b)$, where b is the Compton fraction and A is the uncorrected absorption. This correction does not change the results of the fits but does allow accurate determination of % absorption in the spectra. The correction is necessary because the range of energy deposited in the detector by Compton events extends from 0 to 40 keV, overlapping both the 14 keV and 2 keV energies deposited by the 14 keV gammas.

Run times were 6-48 h for each spectrum, and baseline counts were ~3-15 million after the Compton correction, as needed for reasonable signal-to-noise ratios. Data were collected in 1024 channels and corrected for nonlinearity via interpolation to a linear velocity scale, defined by the spectrum of the 25 μm Fe foil used for calibration. Data were then folded before fitting, using a

This is a preprint, the final version is subject to change, of the American Mineralogist (MSA)
Cite as Authors (Year) Title. American Mineralogist, in press.
DOI: https://doi.org/10.2138/am-2019-7036

206 procedure that folds the spectrum about the channel value that produces the minimum least squares
207 sum difference between the first half of the spectrum and the reflected second half of the spectrum.
208 All Mössbauer data are accessible at http://www.mtholyoke.edu/courses/mdyar/database/.
209
210 Spectra were fitted with 2-3 Lorentzian doublets using the MEX_FielDD program (University of
211 Ghent, courtesy of E. DeGrave). Isomer shifts (IS, or δ), and quadrupole splittings (QS, or Δ) of the
212 doublets were allowed to vary, and widths (full width at half maximum) of all four peaks were
213 coupled to vary in pairs. In a few cases, it was necessary to constrain peak widths to lie above a
214 certain value in order to obtain reasonable parameters, but most spectra were fitted with only the
215 minimal constraints described above.
216
217 Error bars for Mössbauer measurements are discussed by Dyar (1984) and Dyar et al. (2008), with
218 fits to well-resolved spectra having errors of ±0.02 mm/s for IS and QS, and ±3 % absolute on
219 areas. Many of the spectra studied here have multiple overlapping distributions, so the errors are
220 likely slightly higher: ±0.02-0.05 mm/s for IS and QS, with errors of ±3-5 % absolute on areas.
221 Reproducibility (precision) of peak areas based on repeated fits using different constraints (IS, QS,
222 width, and areas constrained in all possible combinations of individual peaks and pairs) and fitting
223 models (Lorentzian, Gaussian, quadrupole splitting distributions) is ±0.3 % absolute for these well-
224 resolved spectra. Accuracy has been determined in previous studies of amphiboles to be ±3-5 %
225 (Dyar 1989) but is highly dependent on the spectrum. This issue is discussed by Dyar et al. (2008).
226
227 Chemical analysis was performed on the samples after the above mentioned chemical and physical
228 treatments to eliminate or reduce other mineral phases. The powders were dried overnight at 110 °C
229 and dissolved by acid attack with HF-$HClO_4$-aqua regia in closed bottles in a microwave oven with
230 or without previous fusion with $LiBO_2$. The solutions were analyzed using inductively coupled
231 plasma-atomic emission spectrometry (ICP-AES, in a Thermo iCap 6500 Duo). Analytical errors

This is a preprint, the final version is subject to change, of the American Mineralogist (MSA)
Cite as Authors (Year) Title. American Mineralogist, in press.
DOI: https://doi.org/10.2138/am-2019-7036

were 1-7 wt% relative to the element oxide results for major elements (average of 4 wt%). The chemical analyses were corrected for non-clay mineral phases that had not been removed in the original treatment and then converted to structural formulas on the basis of $O_{10}(OH)_2$ (Cuadros et al. 2013). The proportion of Fe(II) was taken from Mössbauer spectroscopy. Mössbauer and infrared spectroscopy (mid-infrared, see Cuadros et al. 2013) were used as guides for allocation of Fe and Al between the tetrahedral and octahedral sheets. Here we present only the samples for which there are Mössbauer data, because this technique provides more direct evidence than infrared spectroscopy. Magnesium was allocated to the octahedral sheet. After calculation of the structural formula, the difference between layer charge and interlayer cation charge was 0.0015 (per $O_{10}[OH]_2$) in one case and <0.0008 in the rest, which indicates reliable formulas.

Data from the literature

The data from Cuadros et al. (2013) (only those for which there are Mössbauer results) were completed with others from the literature. For this, articles were selected in which chemical and spectroscopic investigation of Fe-rich 2:1 phyllosilicates had been carried out. The goal was to collect reliable distributions of Fe(III) between the tetrahedral and octahedral sheet, for which reason the results were scrutinized and only those that appeared sufficiently reliable were used. The criteria for the selection were the following. Spectroscopic data were required that provide direct evidence for tetrahedral Fe(III) (e.g., Mössbauer, XANES, EXAFS), rather than other indirect evidence (e.g., octahedral cation pairs from infrared spectroscopy). Because Mössbauer data have been difficult to interpret due to peak overlap, low tetrahedral Fe(III) content and doubtful peak assignment (see introduction), data were mainly selected from rather recent articles, for which the accumulated experience of Mössbauer spectra fitting and interpretation guarantees reliable results, or articles also providing evidence from XANES and/or EXAFS spectroscopies. Some other data were collected from Mössbauer results indicating abundant tetrahedral Fe(III), less likely to have significant errors, and from synthetic samples with no Al, which simplifies the issue of Fe(III)

This is a preprint, the final version is subject to change, of the American Mineralogist (MSA)
Cite as Authors (Year) Title. American Mineralogist, in press.
DOI: https://doi.org/10.2138/am-2019-7036

tetrahedral occupancy. Data were not used from Mössbauer data where the authors indicated significant uncertainty about tetrahedral Fe(III) occupancy or where different authors had obtained significantly different Mössbauer spectra from the same samples, or interpreted the same spectra in a significantly different manner. The structural formulas from all studies were checked for consistency. Data were used only if the layer charge from the lattice cations differed ≤0.03 per $O_{10}(OH)_2$ from the charge of the interlayer cations (typically the difference was <0.01). Some samples have been investigated in two studies and appear twice. In studies where many different samples provided very similar results (chemistry and Fe[III] tetrahedral occupancy) a selection was made that represented the ranges of values obtained.

RESULTS

XRD data

The samples investigated by Cuadros et al. (2013) can be grouped in four classes: nontronite (N), interstratified glauconite-nontronite (G-N), interstratified talc-nontronite (T-N), and interstratified talc-saponite (T-S). T-S samples have higher crystal order than the other groups (Fig. 2; Cuadros et al. 2013). The proportion of the several phyllosilicates was calculated from modeling of the XRD patterns of the oriented mounts (Table 1; for full details see Cuadros et al. 2013). The number of phases (endmember or interstratified) in each sample ranged from 1 to 4. Only the overall proportions of smectite (nontronite or saponite) versus the non-expandable (glauconite or talc) phyllosilicates are reported here (Table 1). The measured positions of the 060 peaks were in good agreement with the phase determination from the oriented mounts. The T-N samples are special because they are interstratified phases with trioctahedral (talc) and dioctahedral (nontronite) layers. Their crystal chemistry is complicated because they have Fe(III) in excess of what the expandable (nontronite) layers can admit, which indicates the existence of nontronite domains within talc layers (Cuadros et al. 2013). In any case, they have two 060 peaks, corresponding to talc and nontronite, except in the case of Va3-413KH (150-153), where the talc peak at 1.536 Å is asymmetric with a

This is a preprint, the final version is subject to change, of the American Mineralogist (MSA)
Cite as Authors (Year) Title. American Mineralogist, in press.
DOI: https://doi.org/10.2138/am-2019-7036

shoulder towards the high-angle side that may correspond to the nontronite peak. Notice that the positions of the 060 peaks were re-visited for this contribution (Table 1) and some are slightly modified from those in Cuadros et al. (2013).

Mössbauer spectra

The Mössbauer spectra were dominated by octahedral Fe(III) doublets (Fig. 3, Table 2). Most samples displayed two doublets, as is typical in phyllosilicates, most likely generated by octahedron distortions due to local chemical and structural modifications (Drits et al. 1997). The spectra indicated a variable range of octahedral Fe(II), higher in the trioctahedral T-S samples, as expected. Also variable was the amount of tetrahedral Fe(III) (Table 1), although Figure 3 displays spectra with significant tetrahedral Fe(III) only. Two samples contained magnetite (M64/1 139GTV-5E [Turtle Pits] and Va3-413KH [313-318]), sample 1183-9 contained goethite (not shown; see Cuadros et al. 2013), and sample Va3-413KH (382-389) contained hematite (Fig. 3, Table 2; Cuadros et al. 2013). These and other trace minerals were accounted for in the calculation of the phyllosilicate compositions (Cuadros et al. 2013). The Mössbauer data allowed determination of Fe(III)/Fe(II) ratios and distribution of Fe(III) between tetrahedral and octahedral sites; these were then checked for consistency with the mid-infrared data of Cuadros et al. (2013).

Structural formulas and tetrahedral Fe(III) occupancy

The structural formulas of samples from Cuadros et al. (2013) and from the literature are divided in four groups (Table 1). The first group is that of nontronite, where there is also one Fe-pyrophyllite, which does not belong in any group but is arguably most related to the nontronite class. The second group is that of dioctahedral micaceous minerals, with glauconite, celadonite and G-N. This group is labeled as G-N because most samples are glauconite-nontronite. The third group is that of T-N, and contains only samples from Cuadros et al. (2013), not surprisingly because this type of interstratified mineral is probably both rare and difficult to identify. Some reports exist of

This is a preprint, the final version is subject to change, of the American Mineralogist (MSA)
Cite as Authors (Year) Title. American Mineralogist, in press.
DOI: https://doi.org/10.2138/am-2019-7036

310 interstratified trioctahedral-dioctahedral phases (e.g., kaolinite-biotite by Ahn and Peacor 1987;
311 biotite-beidellite by Aoudjit et al. 1995; phlogopite-beidellite by Aldega et al. 2009) but with no
312 spectroscopic data on Fe valence or location. The last group is that of trioctahedral specimens, with
313 T-S samples from Cuadros et al. (2013), Fe-rich saponites, Fe-rich talc, and Fe-micas. The reason to
314 group all these minerals in one single trioctahedral group will become evident in the discussion.
315 Within each of the four groups, samples are arranged from low to high tetrahedral Fe(III) (Table 1).
316 The positions of the XRD 060 peaks are included, where available (Table 1).
317
318 The plot of total Fe vs. tetrahedral Fe(III) content using all samples from Cuadros et al. (2013) (Fig.
319 1) shows a control on Fe(III) tetrahedral occupancy by the total Fe content, and that this control is
320 different depending on the trioctahedral / dioctahedral nature of the 2:1 phyllosilicates. The same
321 plot was developed for the samples gathered in this contribution (Fig. 4a). The differences are the
322 addition of samples from the literature and the elimination of those samples from Cuadros et al.
323 (2013) for which there were no Mössbauer data.
324
325 The trioctahedral samples showed a variable behaviour. Some displayed no tetrahedral Fe(III) in a
326 wide range of total Fe content (0.5-2.4 Fe atoms per $O_{10}[OH]_2$; Fig. 4a). Many others, however,
327 displayed a broad trend of increasing tetrahedral Fe(III) with increasing total Fe content. One single
328 correlation was calculated for those samples with tetrahedral Fe(III), except the two specimens with
329 tetrahedral Fe(III) > 0.8 atoms per $O_{10}[OH]_2$ (Fig. 4a), which appeared to be significant ($R^2 = 0.55$).
330 Altogether, these data suggest that the link between total Fe and tetrahedral Fe(III) in trioctahedral
331 2:1 phyllosilicates is rather loose. A group of samples appear to follow a broad trend of increasing
332 tetrahedral Fe(III) and total Fe, but deviations are possible both below and above it.
333
334 The dioctahedral (N and G-N) and the trioctahedral-dioctahedral specimens (T-N) all have similar
335 behavior when total Fe and tetrahedral Fe(III) are compared (Fig. 4a). There is a threshold of total

This is a preprint, the final version is subject to change, of the American Mineralogist (MSA)
Cite as Authors (Year) Title. American Mineralogist, in press.
DOI: https://doi.org/10.2138/am-2019-7036

Fe needed before Fe(III) can enter tetrahedral sites (red and green "x" data points in Fig. 4a are below the threshold). This threshold lies between 1.63 and 1.88 Fe atoms per $O_{10}(OH)_2$ (Fig. 4a), from which value there is a steep increase of tetrahedral Fe(III) as total Fe increases (green, red and orange circles, Fig. 4a). Although with a similar correlation line, the regression for the T-N samples is not significant ($R^2 = 0.33$). Notice that the two T-N samples with lowest tetrahedral Fe(III) in Figure 1 are not in Figure 4a because no Mössbauer data were available. The absence of these two samples changes the corresponding correlation substantially (orange lines in Figs. 1 and 4a) and they will be discussed below.

The difference in behavior between trioctahedral samples and both dioctahedral and trioctahedral-dioctahedral specimens suggests an important structural control on allowing Fe(III) incorporation into the tetrahedral sheet (discussed at length in the discussion section). Importantly, the trioctahedral lattice dimensions are larger than those of the dioctahedral lattice due to the greater occupancy of the octahedral sheet and the large size of the major Mg^{2+} cation. If such a structural factor operates as a control on tetrahedral Fe(III) occupancy, the comparison between tetrahedral Fe(III) and total Fe (Fig. 4a) does not represent the complete phenomenon because Mg is also an important variable controlling crystal lattice dimensions. Thus, tetrahedral Fe(III) was plotted vs. total Fe + Mg (total Fe = tetrahedral Fe[III] + octahedral Fe[III] + octahedral Fe[II]; Mg = octahedral Mg as the samples lack interlayer Mg, Table 1) (Fig. 4b). This new plot causes small changes in N, G-N and T-S samples (from Fig. 4a) because their Mg content is low. However, the addition of Mg improves the correlation for the T-N samples, which becomes significant ($R^2 = 0.59$; Fig. 4b).

The greatest change after Mg inclusion in the relation takes place in the trioctahedral samples, as expected. In this case, most data points become aligned in a single trend in the range of tetrahedral Fe(III) from 0 to 0.93 atoms per $O_{10}(OH)_2$ (Fig. 4b), with a significant correlation ($R^2 = 0.80$).

This is a preprint, the final version is subject to change, of the American Mineralogist (MSA)
Cite as Authors (Year) Title. American Mineralogist, in press.
DOI: https://doi.org/10.2138/am-2019-7036

DISCUSSION

Preliminary considerations about Fe(III) site distribution

The two main obvious controls on tetrahedral Fe(III) content in 2:1 phyllosilicates are (1) Fe(III) availability during mineral formation and (2) the size of the tetrahedral sites, which must be large enough to accommodate Fe(III). In principle, formation in conditions of high Fe concentration increases the chances that Fe occupies tetrahedral sites. However, while Fe(III) enters tetrahedral sites of 2:1 phyllosilicates, Fe(II) does not. This fact suggests a steric control (tetrahedral radii of Fe[II] = 0.71 Å, of Fe[III] = 0.57; Whittaker and Muntus 1970), most possibly enhanced by the large charge imbalanced produced by Fe(II) for Si substitution in the tetrahedra. Accordingly, even in high Fe concentration media, no tetrahedral Fe(II) will be incorporated, only Fe(III). Thus, no tetrahedral Fe should be expected in 2:1 phyllosilicates formed in reducing environments where only Fe(II) was available. This should be apparent from examination of non-expandable 2:1 phyllosilicates, where Fe(II) is stable against changing redox conditions. These minerals may have high octahedral Fe(II) contents but no tetrahedral Fe(II). However, expanding 2:1 phyllosilicates may not be useful to establish origins in an Fe(II)-rich environment because Fe(II) is not stable against redox conditions change. Any such phase containing significant octahedral Fe(II) will oxidize in surface or near-surface conditions and may recrystallize into a new phase containing both tetrahedral and octahedral Fe(III) (and perhaps residual octahedral Fe[II]). There is evidence of such processes from Badaut et al. (1985), who recovered a trioctahedral Fe(II)-rich smectite from the Atlantis II Deep in the Red Sea that oxidized partially in contact with the atmosphere producing a mixture of nontronite, trioctahedral Fe(II)-rich smectite and Fe(III) oxide. These changes did not happen in a geological environment, but prove that a recrystallization process may take place upon oxidation.

This is a preprint, the final version is subject to change, of the American Mineralogist (MSA)
Cite as Authors (Year) Title. American Mineralogist, in press.
DOI: https://doi.org/10.2138/am-2019-7036

When Fe(III) is available during the formation of 2:1 phyllosilicates, whether or not together with Fe(II), what controls the occupancy of tetrahedral sites by Fe(III)? The greater Fe(III) octahedral occupancy widely found (see sample in Table 1) is indicative that octahedral sites are generally better suited for Fe(III) than tetrahedral sites. This, however, is not a fact of absolute value but is relative to the other cations competing for tetrahedral and octahedral positions, and to the size of the tetrahedral sites. Cardile (1989) discussed evidence that both Fe(III) and Fe(II) occupy tetrahedral sites in spinels, even to their exclusion from octahedral sites, due to the larger tetrahedral sites in spinels as compared to those in phyllosilicates. With respect to cation competition for specific sites in phyllosilicates, it appears that the radius and charge of Si^{+4}, Al^{+3}, Fe^{+3}, Fe^{+2}, and Mg^{+2} only allow Al^{3+} and Fe^{3+} to occupy both tetrahedral and octahedral sites. The relative stability of these two cations in the two sites should be a control for Fe(III) distribution between both sites. The fact that Al is more widely found in tetrahedral sites than Fe(III) in 2:1 phyllosilicates suggests that the combined effects are more favorable to tetrahedral Al than to tetrahedral Fe(III).

Steric control on tetrahedral Fe(III) content

The plot of tetrahedral Fe(III) vs. total Fe (Fig. 4a) indicates that the size of the tetrahedral sites is important in controlling tetrahedral Fe(III) occupation, as argued below. Trioctahedral samples can have tetrahedral Fe(III) at any value of total Fe content, even if very low. This is not the case with the dioctahedral and dioctahedral-trioctahedral samples, which require at least ~1.65 Fe atoms per $O_{10}(OH)_2$ in the octahedral sheet before Fe(III) can occupy tetrahedral sites. Such a threshold value is obtained from the intercept at the abscissa in the equations (1.68 total Fe for N, 1.63 total Fe for G-N, and 1.88 total Fe for T-N; Fig. 4a), of which less weight is given to the value for T-N (1.88 total Fe) because of their low coefficient of determination ($R^2 = 0.33$). For all these samples (N, G-N and T-N), Fe(III) >> Fe(II) (Table 1). The sharp boundary for the admission of Fe(III) in the tetrahedra is interpreted to indicate that a large proportion of octahedral Fe is required to produce a structure with tetrahedral sites large enough to host Fe(III). The octahedral cations in the samples

This is a preprint, the final version is subject to change, of the American Mineralogist (MSA)
Cite as Authors (Year) Title. American Mineralogist, in press.
DOI: https://doi.org/10.2138/am-2019-7036

413 are Fe, Al and Mg, with minor Mn and Ti (Table 1). Their radii in octahedral coordination are Al^{+3}
414 0.535 Å, Fe^{+3} 0.645 Å, Mg^{+2} 0.72 Å, and Fe^{+2} 0.78 Å (Shannon 1976). Thus, Fe(II) (included in the
415 variable total Fe of Fig. 4a) and Mg, together with Fe(III), contribute to expand the crystal structure.
416
417 The plot of tetrahedral Fe(III) vs. total Fe + Mg (Fig. 4b) is the complete representation of the
418 required number of "large" cations in the structure of N, G-N, and T-N samples to allow tetrahedral
419 Fe(III) occupancy. The fact that the R^2 value of the regression for the T-N samples is better in
420 Figure 4b than in Figure 4a is in good agreement with the conclusion that octahedral Mg contributes
421 to facilitating tetrahedral Fe(III) occupancy. The total number of large octahedral cations required is
422 1.69 atoms per $O_{10}(OH)_2$ for N, 1.89 atoms for G-N, and 1.79 atoms for G-N (intercept at the
423 abscissa in Fig. 4b). From the average between these three values and the average octahedral
424 occupancy of the corresponding samples (2.02 atoms per $O_{10}[OH]_2$, Table 1), the structural
425 requirement for tetrahedral Fe(III) presence is that 5.3 atoms out of 6 in the octahedral sheet are Fe
426 or Mg, rather than Al. A similar calculation, based instead on the smallest of the intercept values
427 (1.69 atoms per $O_{10}[OH]_2$, from N samples, with average octahedral occupancy of 2.00 atoms;
428 Table 1) produces the same result, where 5.1 atoms out of 6 atoms must be Fe or Mg. The
429 significance of this number is that, on average, five in each ring of six octahedra must be occupied
430 by Fe or Mg (Fig. 5). The larger dimensions of the Mg- and Fe-occupied octahedra cause a
431 concomitant increase of the dimensions of the tetrahedra (Fig. 6). The minimum size to allow
432 Fe(III) in the tetrahedra is reached when five out of six octahedra sites are occupied by Mg or Fe (or
433 Mn or other large cation). Synthetic Si-Fe and Si-Fe-Al nontronites (Petit et al. 2015; Baron et al.
434 2016) fit our regression but are not included here as tetrahedral Fe(III) was based on or supported
435 by IR data, an indirect method of assessing tetrahedral composition.
436
437 Above the threshold, there is a rapid increase of tetrahedral Fe(III) with increasing Fe in the
438 structure (Fig. 4a). From the average value of the three slopes in the plot, 0.73 out of each Fe atom

This is a preprint, the final version is subject to change, of the American Mineralogist (MSA)
Cite as Authors (Year) Title. American Mineralogist, in press.
DOI: https://doi.org/10.2138/am-2019-7036

439 above the threshold are in the tetrahedral sheet. Notice again that most Fe in samples N, G-N and T-
440 N is Fe(III) (Table 1). Thus, after the threshold, Fe(III) preferentially occupies tetrahedral sites,
441 perhaps because of the relative stability of Al and Fe(III) in tetrahedral and octahedral sites of the
442 expanded lattice dimensions of the 2:1 phyllosilicate.
443
444 Further experimental evidence of the steric control on tetrahedral Fe(III) abundance was sought by
445 investigating the *b* dimension of the crystal lattice in the samples. The position of the 060 peak
446 system provides the approximate value of the lattice *b* parameter. A plot of 060 values versus
447 tetrahedral Fe(III) shows that dioctahedral and trioctahedral samples are in different areas, although
448 two nontronite samples are in an intermediate position and one nontronite within the trioctahedral
449 space (Fig. 7). It has been recognized before that nontronite can have 060 values overlapping those
450 of trioctahedral 2:1 phyllosilicates (e.g., 1.521 Å from Brindley 1980; 1.522-1.535 Å from Russell
451 and Clark 1978, and Cuadros et al. 2013). All T-N samples except one have two 060 maxima (Fig.
452 7). There is no meaningful correlation between tetrahedral Fe and the 060 peak positions either for
453 dioctahedral or trioctahedral samples, although a broad trend is apparent for the trioctahedral
454 specimens. However, the *b* parameter represents only one dimension of the crystal lattice, and does
455 not necessarily provide a full description of the size expansion of tetrahedral sites. Figure 6
456 illustrates that the length increase of the sides of the octahedra along the *b* direction (stretching
457 black arrows 1) contributes greatly to increase the side length of the tetrahedra (red arrows).
458 However, also significant is the contribution of the length increase of sides with a smaller
459 component in the *b* direction (black arrows 2, 3, 4; Fig. 6). In addition, the octahedra are more
460 distorted than appear in Figure 6 (e.g., Bailey 1984). Further unlocking between the *b* dimension
461 and tetrahedral site size is produced by other fitting mechanisms between tetrahedral and octahedral
462 sheets, such as tetrahedral rotation and tilt, and changes in octahedral sheet thickness (e.g., Bailey
463 1984).
464

This is a preprint, the final version is subject to change, of the American Mineralogist (MSA)
Cite as Authors (Year) Title. American Mineralogist, in press.
DOI: https://doi.org/10.2138/am-2019-7036

Contrary to these results, Russell and Clark (1978) found a very good correlation between the *b* parameters of several montmorillonites and nontronites and their octahedral and tetrahedral Fe(III) contents, as determined in a previous Mössbauer study by Goodman et al. (1976). Such a result, however, could not be confirmed by other authors for other montmorillonites and nontronites (Cardile 1989), perhaps indicating inaccurate Mössbauer interpretation or a special set of samples used by Goodman et al. (1976) and Russell and Clark (1978). The nontronite samples in the present study were tested for the same plots of Russell and Clark (1978) and produced much weaker correlations ($R^2 \sim 0.5$, not shown) than those found by the previous authors. Including the G-N samples, also dioctahedral, in this test generated still weaker correlations. Notice that some subsets of dioctahedral data points in Figure 7 could produce meaningful correlations. Seemingly, there is a response variability of the *b* dimension to total and tetrahedral Fe(III) increase that may depend on a variety of factors. Although the results of Russell and Clark (1978) have not been reproduced, they were an impressive attempt, perhaps the first, to relate Fe(III) tetrahedral occupancy to the size of the crystal lattice of 2:1 phyllosilicates. Recently reported correlations between tetrahedral Fe(III) and *b* in synthetic samples, specific to Si-Al-Fe nontronites (Petit et al. 2015) or to Si-Fe nontronites (Baron et al. 2016), rather corroborate that such correlations exist only within specific sample groups.

Fe(III) availability during crystallization as control on tetrahedral Fe(III)

The larger dimensions of the crystal lattice of 2:1 trioctahedral phyllosilicates, as compared to dioctahedral ones, imply that there is no steric control on the admission of Fe(III) into their tetrahedra (Fig. 4a). However, it is intriguing that some broad correlation is suggested between total Fe content and tetrahedral Fe(III) for some trioctahedral samples (Fig. 4a). Comparison of tetrahedral Fe(III) with total Fe + Mg (Fig. 4b) suggests that low tetrahedral Fe(III) content is compatible with a range of total Fe + Mg content but that increasing tetrahedral Fe(III) contents occur only where total Fe + Mg > 3 atoms per $O_{10}(OH)_2$ (Fig. 4b). It is unlikely that Mg contributes

This is a preprint, the final version is subject to change, of the American Mineralogist (MSA)
Cite as Authors (Year) Title. American Mineralogist, in press.
DOI: https://doi.org/10.2138/am-2019-7036

to this trend, because there is no steric control on the tetrahedral Fe(III) abundance in trioctahedral samples. Most likely, such a trend is the same of tetrahedral Fe(III) vs. total Fe (Fig. 4a), where the addition of Mg logically squeezes all data points within a narrower range in the x-axis (Fig. 4b).

It was discussed above that the availability of Fe(III) in the formation environment of 2:1 phyllosilicates should be a control on tetrahedral Fe occupancy. A plot of tetrahedral Fe(III) vs. total Fe(III) (octahedral and tetrahedral) of trioctahedral samples provides some confirmation of this hypothesis (Fig. 8a). A broad correlation ($R^2 = 0.66$) results between the two variables. Importantly, in this case all trioctahedral samples are included in the correlation (contrary to Fig. 4a). Most likely, then, the trends of the trioctahedral samples in Figure 4a and 4b are a manifestation of the trend in Figure 8a, which suggests that the only control on tetrahedral Fe(III) in trioctahedral 2:1 phyllosilicates is Fe(III) availability. Further, this correlation suggests that the probability of Fe(III) entering tetrahedral or octahedral sites in trioctahedral phyllosilicates is broadly equal (y-intercept close to zero, slope = 0.68; Fig. 8a). See that if the correlation is forced through y-intercept = 0, the slope becomes 0.55, with $R^2 = 0.63$ (not shown).

It is possible that the values in the plot of tetrahedral Fe(III) vs. total Fe(III) for the trioctahedral phyllosilicates (Fig. 8a) are not those immediately after formation due to later partial oxidation or reduction. The correlation was tested for both smectite samples only, and non-expandable samples only. It was thought that perhaps non-expandable samples (micas and talc), in which Fe oxidation state is more easily preserved, could show a narrower relation between tetrahedral and total Fe(III). This was the case to some extent (Fig. 8b). This result lends support to the hypothesis that total or partial oxidation of octahedral Fe(II) in saponite layers at some stage after mineral formation blurs the link between environmental Fe(III) abundance and Fe(III) distribution between tetrahedral and octahedral sites. The same test for smectite samples produced a non-significant regression of lower slope (not shown).

This is a preprint, the final version is subject to change, of the American Mineralogist (MSA)
Cite as Authors (Year) Title. American Mineralogist, in press.
DOI: https://doi.org/10.2138/am-2019-7036

517

518 The very presence of available Fe(III) to be incorporated to the crystal lattice of trioctahedral or
519 dioctahedral 2:1 phyllosilicates indicates that formation conditions are from intermediate oxic-
520 anoxic (coexistence of Fe[II] and Fe[III]) to oxic (only Fe[III] is present). The solubility of Fe(III)
521 in neutral to alkaline conditions is very low, but there is much evidence from a wide range of
522 environments that Fe(III) is very reactive in poorly-crystalline phases that become precursors of
523 Fe(III)-rich phyllosilicates. Nontronite from submarine hydrothermal settings has been described as
524 forming by the reaction of poorly crystallized Fe(III) oxide and oxy-hydroxide phases with silica
525 adsorbed on their surface (Masuda 1995; Gurvich 2006; Taitel-Goldman et al. 2009; Cuadros et al.
526 2018) or with siliceous tests (Cole 1985). Nontronite in the Columbia River Basalt formed at or
527 near the surface, at temperature < 100 °C and atmospheric pressure by reaction of fluids with the
528 basalt (Baker and Strawn 2014). The altering basalt provided the Si-rich fluids and abundant Fe
529 (rapidly oxidized to Fe[III]) in a non-crystalline matrix. A similar process takes place in the low-
530 temperature, submarine alteration of basaltic glass (Chamley 1989). Silica adsorption and reaction
531 with goethite to produce Fe-rich smectite and nontronite has been described in saline lakes such as
532 Chad (Pédro et al. 1978). Iron-beidellite and nontronite also form in the alkaline B horizons of
533 vertisols (Chamley 1989). During the humid season, Fe, Si and Al are mobilized in the organic-rich
534 A horizon by organic complexing agents. These ions accumulate in the B horizon during the dry
535 season, where they detach from their organic ligands and react to form Fe-beidellite and nontronite
536 (Chamley 1989). The different settings and common reaction elements in all the above
537 environments suggest that the reactions are purely inorganic. However, microbial involvement has
538 been described in some cases and may well accelerate the process by mobilizing Fe(III) into the
539 fluids and acting as nucleation points (Ueshima and Tazaki 2001).

540

541 **The special case of dioctrahedral-trioctahedral 2:1 phyllosilicates**

This is a preprint, the final version is subject to change, of the American Mineralogist (MSA)
Cite as Authors (Year) Title. American Mineralogist, in press.
DOI: https://doi.org/10.2138/am-2019-7036

The T-N samples are special in that they are made up of dioctahedral and trioctahedral domains. Cuadros et al. (2013) showed that the talc (non-expandable) layers of T-N do not correspond exactly to the trioctahedral domains. There is an excess of octahedral Fe(III) in the submarine hydrothermal T-N samples indicating that there are nontronite domains within talc layers. In other words, there is more Fe(III) than indicated by the proportion of (expandable) nontronite, and some of this Fe(III) must be in the (non-expandable) talc layers. This is possible because the layers (or TOT units: tetrahedral-octahedral-tetrahedral) in interstratified 2:1 phyllosilicate phases are "polar" (Lagaly 1979; Güven 1991). This means that the expandable and non-expandable units are defined by the sequence tetrahedral-interlayer-tetrahedral (TIT), which have a homogeneous composition, while the TOT units may be heterogeneous, with T sheets of different composition (Cuadros et al. 2013). Because there may be a composition change across the TOT units, the O sheet can also have a composition intermediate between those of the two types of interstratified layers (Cuadros 2012 and references therein; Cuadros et al. 2013).

Cuadros et al. (2013) investigated two samples of terrestrial origin containing dioctahedral and trioctahedral layers in separate phases, with no or very little layer interstratification. These samples were CRB-03-026, a mixture of celadonite (a proportion of 75% as determined from XRD modeling of oriented mounts) and saponite (25%); and Nontronite 51, a mixture of nontronite (75%) and interstratified T-N (with 95% talc layers and 5% nontronite layers). Because these two samples have no or very minor interstratification, they contain no or very few polar layers, and their chemical data exactly match the relative proportions of expandable (saponite, nontronite) and non-expandable (celadonite, talc) components (Cuadros et al. 2013). These are the two "T-N, Cel" samples in Figure 1 at total Fe ~1.25 atoms per $O_{10}(OH)_2$. They most likely have a different behaviour from that of the other T-N specimens, which are interstratified talc-nontronite. The correlation of all "TN, Cel" samples is good ($R^2 = 0.89$; Fig. 1) but this may be deceptive for two reasons. First, the two terrestrial samples plot separately from the true T-N samples. Second, the

This is a preprint, the final version is subject to change, of the American Mineralogist (MSA)
Cite as Authors (Year) Title. American Mineralogist, in press.
DOI: https://doi.org/10.2138/am-2019-7036

568 true T-N samples appear to align along a different line from that of the regression of all "T-N, Cel"
569 samples (Fig. 1). The meaningful correlation of tetrahedral Fe(III) vs. total Fe + Mg ($R^2 = 0.59$, Fig.
570 4b) suggests that indeed submarine hydrothermal T-N samples are a set behaving coherently and
571 separately from the two terrestrial dioctahedral-trioctahedral samples.
572
573 This conclusion is further supported by the following considerations. The two terrestrial samples
574 contain fully dioctahedral layers and fully trioctahedral layers that are not interstratified and thus
575 not connected in the crystals. This means that the trioctahedral layers within these two samples have
576 no steric restrictions to tetrahedral Fe(III). At the same time, the dioctahedral layers within these
577 samples have the steric control described above (5 atoms within each ring of 6 must be Fe or Mg).
578 The plot of total Fe vs. tetrahedral Fe(III) (Fig. 1) must then produce data points falling between
579 those of trioctahedral and dioctahedral samples, which is exactly the result for the two terrestrial "T-
580 N, Cel" samples (Total Fe ~1.25 atoms per $O_{10}[OH]_2$, Fig. 1). Such an intermediate value does not
581 have a physical meaning representing steric control on tetrahedral Fe(III) abundance, but rather it is
582 the average between values from layers with no steric control (trioctahedral layers) and layers with
583 steric control (dioctahedral). The true interstratified T-N samples, however, fall within the group of
584 the dioctahedral samples (N, G-N; Figs. 1 and 4).This is because their octahedral sheets are either
585 totally or partially nontronite-like (dioctahedral) in composition, which causes them to behave as
586 dioctahedral samples with respect to steric control on tetrahedral Fe(III) content. The proportion of
587 expandable layers (or nontronite) measured with XRD in these samples ranged 60-80% (Table 1).
588 Thus, the fraction of dioctahedral domains in these samples amounts to 60-80% plus the nontronite
589 domains within non-expandable (or talc) layers. Consequently, the submarine hydrothermal T-N
590 samples are dominantly dioctahedral and it is reasonable that they plot with N and G-N samples.
591
592 The plot of total Fe(III) vs. tetrahedral Fe(III) (Fig. 8a) shows curious behavior for the T-N samples,
593 which appear along a tight negative correlation (Fig. 8a). This seems counterintuitive, because

This is a preprint, the final version is subject to change, of the American Mineralogist (MSA)
Cite as Authors (Year) Title. American Mineralogist, in press.
DOI: https://doi.org/10.2138/am-2019-7036

greater availability of Fe(III) is expected to result in greater tetrahedral Fe(III) occupancy. However, such is the case for entirely trioctahedral samples only, because they do not have steric restrictions (Fig. 8a). Samples T-N have steric restrictions because they are dominantly dioctahedral. For them, total Fe(III) is a proxy for the proportion of dioctahedral (nontronite) domains, because Fe(III) is more abundant in these domains than in trioctahedral talc domains. The greater the proportion of nontronite domains, the greater the sample proportion having steric control on Fe(III) occupancy, and thus the less tetrahedral Fe(III). In other words, the negative correlation in Figure 8a is ultimately between tetrahedral Fe(III) and nontronite domain volume in the samples. In summary, the overall proportion of trioctahedral domains in each T-N sample is so small that they behave as dioctahedral (Fig. 4), but the range of dioctahedral-to-trioctahedral domain volume covered by these samples is manifested in a negative correlation between tetrahedral Fe(III) and the volume of nontronite domains (Fig. 8a).

Maximum tetrahedral Fe(III) content

The maximum values of tetrahedral Fe(III) in this study are found in two trioctahedral samples, with 0.93 and 0.86 atoms per $O_{10}(OH)_2$, both phlogopites from the same locality, followed by 0.75 atoms per $O_{10}(OH)_2$, in a nontronite, and 0.66 atoms per $O_{10}(OH)_2$, in a T-N with 80% of nontronite layers (Table 1, Figure 4). Higher values are possible, for example that reported by Filut et al. (1985) for a specimen of anandite with the formula $Si_{2.60}Fe(III)_{1.40}$ $[Al_{0.10}Fe(III)_{0.28}Fe(II)_{2.01}Mg_{0.46}Mn(III)_{0.04}Mn(II)_{0.04}Ti_{0.01}]$ $Ba_{0.96}K_{0.03}Na_{0.01}$ $O_{10}(OH)F_{0.04}S_{0.84}Cl_{0.16}$. This sample was not used in the present study because the oxidation state of Mn was assumed and there is a charge imbalance in the formula. Trioctahedral brittle micas are probably the 2:1 phyllosilicates that can reach highest tetrahedral Fe(III) occupancy because the layer charge is highest of all micas, allowing higher Fe(III)-for-Si-substitution, and they typically form in environments with higher Fe/Al ratio than their dioctahedral counterparts. Accordingly, maximum tetrahedral Fe(III) occupancy may be ~1.5 atoms per $O_{10}(OH)_2$. However, such high values can

This is a preprint, the final version is subject to change, of the American Mineralogist (MSA)
Cite as Authors (Year) Title. American Mineralogist, in press.
DOI: https://doi.org/10.2138/am-2019-7036

620 probably be reached only in environments of extremely high Fe(III)/Si+Al abundance. The large
621 difference between the tetrahedral radii of Fe(III) and Si (0.57 and 0.26 Å, respectively; Whittaker
622 and Muntus 1970; Shannon 1976) implies that high Fe(III)-for-Si substitution sets strain on the
623 lattice, such that Fe(III) can compete successfully for tetrahedral sites only where Si and Al are in
624 low abundance.
625
626 The anandite of Filut et al. (1985), with tetahedral Fe(III) of 1.40 and total Fe(III) of 1.70 atoms per
627 $O_{10}(OH)F_{0.04}S_{0.84}Cl_{0.16}$ would plot well above the line for the trioctahedral samples in Figure 8a.
628 This stresses that the distribution of Fe(III) between octahedral and tetrahedral sites in trioctahedral
629 2:1 phyllosilicates is approximate to 50% only on average, because chemical and structural
630 constraints modify it widely.
631

632 **IMPLICATIONS**

633 Our model of tetrahedral Fe(III) control on 2:1 phyllosilicates establishes important chemical-
634 structural relationships that have been long sought. The model enables prediction of Fe(III)
635 distribution between structural sites, after the sample mineralogy has been established, with only
636 chemical data, removing an important crystal-chemical uncertainty from studies not including
637 spectroscopic data. The model also allows further exploration of the thermodynamic stability of
638 phyllosilicates including cationic size considerations. Such an approach may prove helpful to
639 further our understanding of the factors controlling the stability of minerals with complex and
640 variable composition. Iron-rich phyllosilicates are the most reactive and so very significant for
641 geochemical and biological processes. Our model will help to better link mineral stability/reactivity
642 to Fe bio-geochemical cycles.
643

644 **ACKNOWLEDGMENTS**

645 Study funded by the IEF Marie Curie program of the EC (Hydro-Mars). E.A. Breves and M. Nelms
646 are thanked for help with Mössbauer data processing. The comments of A. Baldermann and an
647 anonymous reviewer greatly helped to improve this article.

This is a preprint, the final version is subject to change, of the American Mineralogist (MSA)
Cite as Authors (Year) Title. American Mineralogist, in press.
DOI: https://doi.org/10.2138/am-2019-7036

References

Ahn, J.H., and Peacor, D.R. (1987) Kaolinitization of biotite: TEM data and implications for an alteration mechanism. American Mineralogist, 72, 353-356.

Aldega, L., Cuadros, J., Laurora, A., and Rossi, A. (2009) Weathering of phlogopite to beidellite in a karstic environment. American Journal of Science, 309, 689-710.

Andrews, A.J., Dollase, W.A., and Fleet, M.E. (1983) A Mössbauer study of saponite in Layer 2 Basalt, Deep Sea Drilling Project Leg 69. DSDP vol. LXIX, n. 31, 585-588. http://deepseadrilling.org/69/dsdp_toc.htm

Aoudjit, H., Robert, M., Elsass, F., and Curmi, P. (1995) Detailed study of smectite genesis in granicitc saprolites by analytical electron microscopy. Clay Minerals, 30, 135-147.

Badaut, D., Besson, G., Decarreau, A., and Rautureau, R. (1985) Occurrence of a ferrous, trioctahedral smectite in recent sediments of Atlantis II Deep, Read Sea. Clay Minerals, 20, 389-404.

Bailey, S.W. (1984) Crystal chemistry of the true micas. In: S.W. Bailey, Eds., Micas,13, pp. 13-60. Reviews in Mineralogy, Mineralogical Society of America, Chantilly, Virginia.

Baker, L.L., and Strawn, D.G. (2014) Temperature effects on the crystallinity of synthetic nontronite and implications for nontronite formation in Columbia River Basalts. Clays and Clay Minerals, 62, 89-101.

674 Baldermann, A., Dohrmann, S., Kaufhold, S., Nickel, C., Letofsky-Papst, I., and Dietzel, M. (2014)
675 The Fe-Mg-saponite solid solution series – a hydrothermal synthesis study. Clay Minerals, 49, 391–
676 415.
677
678 Baldermann, A., Warr, L.N., Letofsky-Papst, I., and Mavromatis, V. (2015) Substantial iron
679 sequestration during green-clay authigenesis in modern deep-sea sediments. Nature Geoscience, 8,
680 885-889.
681
682 Baron, F., Petit, S., Tertre, E., and Decarreau, A. (2016) Influence of aqueous Si and Fe speciation
683 on tetrahedral Fe(III) substitutions in nontronites: a clay synthesis approach. Clays and Clay
684 Minerals, 64, 230-244.
685
686 Besson, G., and Drits, V.A. (1997) Refined relationships between chemical composition of
687 dioctahedral fine-grained micaceous minerals and their infrared spectra within the OH stretching
688 region. Part II: The main factors affecting OH vibrations and quantitative analysis. Clays and Clay
689 Minerals, 45, 170-183.
690
691 Brigatti, M.F., Lalonde, A.E., and Medici, L. (1999) Crystal chemistry of $^{IV}Fe^{3+}$-rich phlogopites: A
692 combined single-crystal X-ray and Mössbauer study. In H. Kodama, A.R. Mermut, and J.K.
693 Torrance Eds., Clays for Our Future. Proceedings of the 11th International Clay Conference,
694 Ottawa, Canada, 1997, p. 317-326. ICC97 Organizing Committee, Ottawa.
695
696 Brindley, G.W. (1980) Order-disorder in clay mineral structures. In: G.W. Brindley, and G. Brown,
697 Eds., Crystal Structures of Clay Minerals and their X-Ray Identification. Monograph no. 5,
698 Mineralogical Society, London, pp. 125-196.
699

Cardile, C.M. (1989) Tetrahedral iron in smectite: A critical commentary. Clays and Clay Minerals, 37, 185-188.

Chamley, H. (1989) Clay Sedimentology. Springer-Verlag, Berlin.

Coey, J.M.D., Chukhrov, F.V., and Zvyagin, B.B. (1984) Cation distribution, Mössbauer spectra, and magnetic properties of ferripyriphyllite. Clays and Clay Minerals, 32, 198-204.

Cole, T.G. (1985) Composition, oxygen isotope geochemistry, and origin of smectite in the metalliferous sediments of the Bauer Deep, southeast Pacific. Geochimica et Cosmochimica Acta, 49, 221-235.

Cuadros, J. (2012) Clay crystal-chemical adaptability and transformation mechanisms. Clay Minerals, 47, 147-164.

Cuadros, J. (2017) Clay minerals interaction with microorganisms: a review. Clay Minerals, 52, 235-261. DOI: https://doi.org/10.1180/claymin.2017.052.2.05

Cuadros, J., Andrade, G., Ferreira, T.O., Partiti, C.S.M., Cohen, R., and Vidal-Torrado, P. (2017) The mangrove reactor: fast clay transformation and potassium sink. Applied Clay Science, 140, 50-58. DOI: http://dx.doi.org/10.1016/j.clay.2017.01.022

Cuadros, J., Michalski, J.R., Dekov, V., Bishop, J., Fiore, S., and Dyar, M.D. (2013) Crystal-chemistry of interstratified Mg/Fe-clay minerals from seafloor hydrothermal sites. Chemical Geology, 360-361, 142-158. DOI: http://dx.doi.org/10.1016/j.chemgeo.2013.10.016

726 Cuadros, J., Michalski, J.R., Dekov, V., and Bishop, J.L. (2016) Octahedral chemistry of 2:1 clay
727 minerals and hydroxyl band position in the near-infrared. Application to Mars. American
728 Mineralogist, 101, 554-563. DOI: http://dx.doi.org/10.2138/am-2016-5366
729
730 Cuadros, J., Šegvić, B., Dekov, V., Michalski, J.R., and Baussà Bardají, D. (2018) Electron
731 microscopy investigation of the genetic link between Fe oxides/oxyhydroxides and nontronite in
732 submarine hydrothermal fields. Marine Geology, 395, 247-259.
733
734 Decarreau, A., Petit, S., Martin, F., Farges, F., Vieillard, P., and Joussein, E. (2008) Hydrothermal
735 synthesis, between 75 and 150 °C, of high-charge, ferric nontronites. Clays and Clay Minerals, 56,
736 322-337.
737
738 Dong, H., Jaisi, D., Kim, J., and Zhang, G. (2009) Microbe-clay mineral interactions. American
739 Mineralogist, 94, 1505-1519.
740
741 Drits, V., Dainyak, L., Muller, F., Besson, G., and Manceau, A. (1997) Isomorphous cation
742 distribution in celadonites, glauconites and Fe-illites determined by infrared, Mösbauer and EXAFS
743 spectroscopies. Clay Minerals, 32, 153-179.
744
745 Dyar, M.D. (1984) Precision and interlaboratory reproducibility of measurements of the Mössbauer
746 effect in minerals. American Mineralogist, 69, 1127-1144.
747
748 Dyar, M.D. (1987) A review of Mössbauer data on trioctahedral micas: Evidence for tetrahedral
749 Fe^{3+} and cation ordering. American Mineralogist, 72, 102-112.
750

751 Dyar, M.D. (1990) Mössbauer spectra of biotite from metapelites. American Mineralogist, 75, 656-
752 666.
753
754 Dyar, M.D. (2002) Optical and Mössbauer spectroscopy of iron in micas. In A. Mottana, F.P. Sassi,
755 J.B. Thompson, S. Guggenheim Eds., Micas: Crystal Chemistry and Metamorphic Petrology, 46, p.
756 313-349. Reviews in Mineralogy and Geochemistry, Mineralogical Society of America,
757 Washington, and Accademia Nazionale dei Lincei, Rome.
758
759 Dyar, M.D., and Burns, R.G. (1986) Mössbauer spectral study of ferruginous one-layer
760 trioctahedral micas. American Mineralogist, 71, 955-969.
761
762 Dyar, M.D., McGuire, A.V., and Ziegler, R.D. (1989) Redox equilibria and crystal chemistry of
763 coexisting minerals from spinel lherzolite mantle minerals. American Mineralogist, 74, 969-980.
764
765 Dyar, M.D., Schaefer, M.W., Sklute, E.C., and Bishop, J.L. (2008) Mössbauer spectroscopy of
766 phyllosilicates: Effects of fitting models on recoil-free fractions and redox ratios. Clay Minerals, 43,
767 3-33.
768
769 Fialips, C.-I., Huo, D., Yan, L., Wu, J., and Stucki, J. (2002) Infrared study of reduced and reduced-
770 reoxidized ferruginous smectite. Clays and Clay Minerals, 50, 455-469.
771
772 Filut, M., Rule, A.C., and Bailey, S.W. (1985) Crystal structure refinement of anandite-2*Or*, a
773 barium- and sulfur-bearing trioctahedral mica. American Mineralogist, 70, 1298-1308.
774
775 Gates, W.P., Slade, P.G., Manceau, A., and Lanson, B. (2002) Site occupancies by iron in
776 nontronites. Clays and Clay Minerals, 50, 223-239.

Goodman, B.A., Russell, J.D., Fraser, A.R., and Woodhams, F.W.D. (1976) A Mössbauer and IR spectroscopic study of the structure of nontronite. Clays and Clay Minerals, 24, 53-59.

Grauby, O., Petit, S., Decarreau, A., and Baronnet, A. (1994) The nontronite-saponite series: An experimental approach. European Journal of Mineralogy, 6, 99-112.

Gurvich, E.G. (2006) Metalliferous Sediments of the World Ocean. Springer, Berlin.

Güven, N. (1991) On a definition of illite/smectite mixed-layer. Clays and Clay Minerals, 39, 661-662.

Hekinian, R., Hoffert, M., Larqué, P., Cheminée, J.L., Stoffers, P., and Bideau, D. (1993) Hydrothermal Fe and Si oxyhydroxide deposits from South Pacific intraplate volcanoes and East Pacific Rise axial and off-axial regions. Economic Geology, 88, 2099-2121.

Jaisi, D.P., Kukkadapu, R.K., Eberl, D.D., and Dong, H. (2005) Control of Fe(III) site occupancy on the rate and extent of microbial reduction of Fe(III) in nontronite. Geochimica et Cosmochimica Acta, 69, 5429-5440.

Köster, H., Ehrlicher, H., Gilg, H., Jordan, R., Murad, E., and Onnich, K. (1999) Mineralogical and chemical characteristics of five nontronites and Fe-rich smectites. Clay Minerals, 34, 579-599

Kotlicki, A., Szczyrba, J., and Wiewióra, A. (1981) Mössbauer study of glauconites from Poland. Clay Minerals, 16, 221-230.

803 Lagaly, G. (1979) The layer charge of regular interstratified 2:1 clay minerals. Clays and Clay
804 Minerals, 27, 1-10.
805
806 Long, G.J., Cranshaw, T.E., and Longworth, G. (1983) The ideal Mössbauer effect absorber
807 thicknesses. Mössbauer Effect Reference Data Journal, 6, 42-49.
808
809 Manceau, A., Lanson, B., Drits, V., Chateigner, D., Gates, W., Wu, J., Huo, D., and Stucki, J.
810 (2000) Oxidation-reduction mechanism of iron in dioctahedral smectites: I. Crystal chemistry of
811 oxidized reference nontronites. American Mineralogist, 85, 133-152.
812
813 Martin, F., Micoud, P., Delmotte, L., Marichal, C., Le Dred, R., De Parseval, P., Mari, A., Fortuné,
814 J-P., Salvi, S., Béziat, D., Grauby, O., and Ferret, J. (1999) The structural formula of talc from the
815 Trimouns deposit, Pyrenees, France. The Canadian Mineralogist, 37, 997-1006.
816
817 Masuda, H. (1995) Iron-rich smectite formation in the hydrothermal sediment of Iheya Basin,
818 Okinawa Trough. In H. Sakai, and Y. Nozaki Eds., Biogeochemical Processes and Ocean Flux in
819 the Western Pacific, p. 509-521. Terra Scientific Publishing Company, Tokyo.
820
821 Michalski, J.R., Cuadros, J., Bishop, J.L., Dyar, M.D., Dekov, V., and Fiore, S. (2015) Constraints
822 on the crystal-chemistry of Fe/Mg-rich smectitic clays on Mars and links to global alteration trends.
823 Earth and Planetary Science Letters, 427, 215-225. DOI: 10.1016/j.epsl.2015.06.020
824
825 Murad, E., and Wagner, U. (1994) The Mössbauer spectrum of illite. Clay Minerals, 29, 1-10.
826
827 Pédro, G., Carmouze, G.P., and Velde, B. (1978) Peloidal nontronite formation in recent sediments
828 of lake Chad. Chemical Geology, 23, 139-149.

Petit, S., Decarreau, A., Gates, W., Andrieux, P., and Grauby, O. (2015) Hydrothermal synthesis of dioctahedral smectites: The Al-Fe^{3+} chemical series. Part II: Crystal-chemistry. Applied Clay Science, 104, 96-105.

Rancourt, D.G. (1994) Mösbauer spectroscopy of minerals. II. Problem of resolving cis and trans octahedral Fe^{2+} sites. Physics and Chemistry of Minerals, 21, 250-257.

Rancourt, D.G., Dang, M.-Z., and Lalonde, A.E. (1992) Mössbauer spectroscopy of tetrahedral Fe^{3+} in trioctahedral micas. American Mineralogist, 77, 34-43.

Rozenson, I., and Heller-Kallai, L. (1977) Mössbauer spectra of dioctahedral smectites. Clays and Clay Minerals, 25, 94-101.

Russell, J.D., and Clark, D.R. (1978) The effect of Fe-for-Si substitution on the *b*-dimension of nontronite. Clay Minerals, 13, 133-137.

Sánchez-Marañón, M., Cuadros, J., Michalski, J.R., Melgosa, M., and Dekov, V. (2018) Identification of iron in Earth analogues of Martian phyllosilicates using visible reflectance spectroscopy: spectral derivatives and color parameters. Applied Clay Science, 165, 264-276. DOI: https://doi.org/10.1016/j.clay.2018.08.016

Shannon, R.D. (1976) Revised effective ionic radii and systematic studies of interatomic distances in halides and chalcogenides. Acta Crystallographica, A32, 751-767.

Slonimskaya, M., Besson, G., Dainyak, L., Tchoubar, C., and Drits, V. (1986) Interpretation of the IR spectra of celadonites and glauconites in the region of OH-stretching frequencies. Clay Minerals, 21, 377-388.

Stucki, J.W., Lee, K., Zhang, L., and Larson, R.A. (2002) Effects of iron oxidation state on the surface and structural properties of smectites. Pure and Applied Chemistry, 74, 2145–2158.

Taitel-Goldman, N., Ezersky, V., and Mogilyanski, D. (2009) High-resolution transmission electron microscopy study of Fe-Mn oxides in the hydrothermal sediments of the Red Sea Deeps system. Clays and Clay Minerals, 57, 465-475.

Ueshima, M., and Tazaki, K. (2001) Possible role of microbial polysaccharides in nontronite formation. Clays and Clay Minerals, 49, 292-299.

Whittaker, E.J.W., and Muntus, R. (1970) Ionic radii for use in geochemistry. Geochimica et Cosmochimica Acta, 34, 945-956.

Wilson, M.J. (2004) Weathering of the primary rock-forming minerals: processes, products and rates. Clay Minerals, 39, 233-266.

Zaitseva, T.S., Gorokhov, I.M., Ivanovskaya, T.A., Semikhatov, M.A., Kuznetsov, A.B., Mel'nikov, N.N., Arakelyants, M.M., and Yakovleva, O.V. (2008) Mössbauer characteristics, mineralogy and isotopic age (Rb–Sr, K–Ar) of Upper Riphean glauconites from the Uk Formation, the Southern Urals. Stratigraphy and Geological Correlation, 16, 227–247.

This is a preprint, the final version is subject to change, of the American Mineralogist (MSA)
Cite as Authors (Year) Title. American Mineralogist, in press.
DOI: https://doi.org/10.2138/am-2019-7036

Figure captions

Figure 1. Correlation between the tetrahedral Fe (only Fe[III]) and total Fe (tetrahedral Fe[III] + octahedral Fe[III] + octahedral Fe[II]) as atoms per $O_{10}(OH)_2$ from the samples in Cuadros et al. (2013), as shown by Sánchez-Marañón et al. (2018). Three groups are defined, trioctahedral samples (interstratified talc-saponite, T-S), dioctahedral-trioctahedral specimens (interstratified talc-nontronite, mixture of celadonite with saponite, mixture of talc and nontronite, labeled "T-N, Cel") and dioctahedral samples (interstratified glauconite-nontronite, G-N). The nontronite data points (N) are not sufficient to define a correlation. The threshold of total Fe content for the occurrence of tetrahedral Fe varies for the type of sample, increasing from trioctahedral to diotahedral-trioctahedral and to dioctahedral.

Figure 2. XRD patterns of the oriented mounts of samples corresponding to each of the representative groups, from air-dry (AD) and ethylene-glycol intercalated (EG) specimens. They are nontronite (N) Cy 82-14-5; glauconite-nontronite (G-N) Va22-146KS (586-587); talc-nontronite (T-N) Va22-146KS (575-577); and talc-saponite (T-S) Va3-413KH (382-389). The peak at 7.4 Å in G-N could correspond to hydrotalcite or Fe-serpentine; if the latter is the case, the calculated amount of serpentine is ~ 2 %. The T-S sample shows traces of hematite (Hem) and mirabilite (Mir) that remained after the purification process; both were accounted for in the calculation of the phyllosilicate composition (Cuadros et al. 2013). The intensity of the XRD patterns of T-S has been reduced to half for a better display.

Figure 3. Mössbauer spectra and their decomposition into the individual components of four samples representative of each group (the same samples as in Fig. 2). They all show significant tetrahedral Fe(III) content. Hematite is present in the T-S sample, corresponding to one of the octahedral Fe(III) components.

This is a preprint, the final version is subject to change, of the American Mineralogist (MSA)
Cite as Authors (Year) Title. American Mineralogist, in press.
DOI: https://doi.org/10.2138/am-2019-7036

Figure 4. Plots of chemical composition vs. tetrahedral Fe(III) content for samples in Table 1. Total Fe indicates Fe(II) + Fe(III), tetrahedral and octahedral. All values are atoms per $O_{10}(OH)_2$. "x" Symbols indicate that the data points were not used in the correlations. Open blue circles indicate synthetic trioctahedral samples, and they are always superimposed on other symbols (i.e., synthetic sample included [dot] or not included in the correlation ["x"]).

Figure 5. Sketch of the octahedral sheet of dioctahedral phyllosilicates showing the minimum amount of large cations (mainly Fe[III or II] and Mg) required to expand the crystal lattice and allow Fe(III) to enter tetrahedral sites. The arrangement of Al- and Mg/Fe-sites at the bottom is perfectly ordered for the sake of simplicity, but there is no need that this is the case.

Figure 6. Sketch of octahedral and tetrahedral sites in phyllosilicates. Green octahedra are occupied by Fe or Mg; the orange octahedron is occupied by Al. The black arrows are examples indicating the direction of growth of the sides of the tetrahedra when occupied by Fe/Mg rather than Al. The size increase of the octahedra produces an increase of the size of the tetrahedra (red arrows; the red arrow within one of the tetrahedra depicts the extension of the side from one of the basal corners to the apical corner shared with the octahedron below). The *b* crystallographic direction is indicated.

Figure 7. Plot of the position of the maximum of the 060 XRD peak system vs. the tetrahedral Fe(III) content, as atoms per $O_{10}(OH)_2$. All T-N samples but one displayed two maxima (one from the dioctahedral domains and one from trioctahedral domains). Open symbols indicate data from the bibliography.

Figure 8. (a) Plot of total Fe(III) (tetrahedral and octahedral) vs. tetrahedral Fe(III) for trioctahedral samples and trioctahedral-dioctahedral samples (T-N). (b) The same plot for trioctahedral, non-

expandable samples; i.e., saponites and saponite-rich samples have been removed. All data are atoms per $O_{10}(OH)_2$.

This is a preprint, the final version is subject to change, of the American Mineralogist (MSA)
Cite as Authors (Year) Title. American Mineralogist, in press.
DOI: https://doi.org/10.2138/am-2019-7036

Table 1. Structural formulas of samples in which Fe(III)/Fe(II) ratios and distribution of Fe(III) between tetrahedral and octahedral sites are from spectroscopic methods; and d-spacing of the 060 peak or peaks.

Type	Mineralogy	Sample	%Di-Sm	%Tri-Sm	Si tet	Al tet	FeIII tet	Al oct	Mg oct	FeIII oct	FeII oct	Mn oct	Ti oct	Σ oct	Fe Tot	TotFe+Mg oct	Mg int	Ca int	Na int	K int	060 (Å)	Reference
Dioct.	Fe-smectite	W Australia	100		3.79	0.21	0.00	0.75	0.20	1.04	0.00	nr	nr	1.98	1.04	1.23	nr	nr	nr	nr		Gates et al. (2002)
Dioct.	Nontronite	SWa-1	100		3.70	0.30	0.00	0.55	0.13	1.31	0.00	nr	nr	1.99	1.31	1.44	nr	nr	nr	nr		Gates et al. (2002)
Dioct.	Nontronite	SWa-1	100		3.69	0.31	0.00	0.53	0.13	1.34	0.01	nr	nr	2.00	1.34	1.47	0.00	0.00	0.44	0.00	1.509	Manceau et al. (2000)
Dioct.	Nontronite	PV	100		3.79	0.22	0.00	0.33	0.24	1.44	0.01	nr	nr	2.00	1.44	1.68	0.00	0.00	0.45	0.00	1.514	Manceau et al. (2000)
Dioct.	Nontronite	Cheney	100		3.53	0.47	0.00	0.50	0.03	1.48	0.00	nr	nr	2.00	1.48	1.50	nr	nr	nr	nr		Gates et al. (2002)
Dioct.	Nontronite	Garfield	100		3.61	0.39	0.00	0.16	0.02	1.82	0.01	nr	nr	2.01	1.83	1.85	0.00	0.00	0.41	0.00	1.521	Manceau et al. (2000)
Dioct.	Nontronite	Giralong	100		3.66	0.32	0.03	0.22	0.14	1.65	0.00	nr	nr	2.01	1.67	1.81	nr	nr	nr	nr		Gates et al. (2002)
Dioct.	Nontronite	NAu-1	100		3.49	0.48	0.04	0.18	0.02	1.81	0.00	nr	nr	2.01	1.84	1.86	nr	nr	nr	nr		Gates et al. (2002)
Dioct.	Nontronite	Garfield	100		3.51	0.44	0.05	0.17	0.02	1.82	0.00	nr	nr	2.00	1.87	1.88	nr	nr	nr	nr		Gates et al. (2002)
Dioct.	Nontronite	Manito	100		3.54	0.41	0.06	0.21	0.06	1.74	0.00	nr	nr	2.01	1.80	1.86	nr	nr	nr	nr		Gates et al. (2002)
Dioct.	Nontronite	Mountainville	100		3.51	0.39	0.11	0.21	0.02	1.77	0.00	nr	nr	2.00	1.88	1.90	nr	nr	nr	nr		Gates et al. (2002)
Dioct.	Nontronite	Hoher Hagen	100		3.65	0.24	0.11	0.00	0.04	1.96	0.02	nd	nd	2.02	2.09	2.13	0.00	0.01	0.35	0.01		Köster et al. (1999)
Dioct.	Nontronite	Bingham	100		3.59	0.30	0.12	0.15	0.12	1.74	0.00	nr	nr	2.00	1.86	1.97	nr	nr	nr	nr		Gates et al. (2002)
Dioct.	Fe-pyrophyllite		0		3.80	0.04	0.16	0.09	0.11	1.87	0.00	nr	nr	2.07	2.03	2.14	0.00	0.05	0.00	0.00	1.517	Coey et al. (1984)
Dioct.	Nontronite	HQ	100		3.49	0.30	0.21	0.26	0.02	1.73	0.00	nr	nr	2.00	1.94	1.95	nr	nr	nr	nr		Gates et al. (2002)
Dioct.	Nontronite	NG-1	100		3.56	0.13	0.31	0.36	0.03	1.61	0.00	nr	nr	2.00	1.92	1.95	nr	nr	nr	nr		Gates et al. (2002)
Dioct.	Nontronite	Nau-2	100		3.56	0.13	0.31	0.36	0.03	1.61	0.00	nr	nr	2.00	1.92	1.95	nr	nr	nr	nr		Gates et al. (2002)
Dioct.	Nontronite	NG-1	100		3.65	0.04	0.32	0.44	0.03	1.54	0.01	nr	nr	2.02	1.86	1.89	0.00	0.00	0.35	0.00	1.522	Manceau et al. (2000)
Dioct.	Nontronite	Spokane	100		3.63	0.02	0.35	0.02	0.02	1.95	0.00	nr	nr	1.98	2.30	2.32	nr	nr	nr	nr		Gates et al. (2002)
Dioct.	Nontronite	Cy 82-14-5	100		3.60	0.04	0.36	0.00	0.28	1.76	0.00	0.00	0.00	2.04	2.12	2.40	0.00	0.03	0.48	0.03	1.517	Cuadros et al. (2013)
Dioct.	Nontronite	1183-15	100		3.62	0.01	0.37	0.00	0.31	1.67	0.00	0.01	0.00	1.99	2.04	2.35	0.00	0.00	0.40	0.31	1.513	Cuadros et al. (2013)
Dioct.	Nontronite	CZ	100		3.52	0.02	0.46	0.12	0.02	1.87	0.00	nr	nr	2.00	2.33	2.35	nr	nr	nr	nr		Gates et al. (2002)
Dioct.	Nontronite	Synthetic	100		3.25	0.00	0.75	0.00	0.00	2.00	0.00	0.00	0.00	2.00	2.75	2.75	0.00	0.00	0.75	0.00	1.540	Decarreau et al. (2008)
Dioct.	G-N	Va22-146KS (1145-1146)	47		3.95	0.05	0.00	0.04	0.25	1.65	0.05	0.00	0.00	1.99	1.70	1.95	0.00	0.01	0.11	0.24	1.510	Cuadros et al. (2013)

Dioct.	Celadonite	Celadonite 69	0		3.94	0.06	0.00	0.05	0.41	1.15	0.36	nr	nr	1.97	1.51	1.92	0.00	0.03	0.01	0.83	1.512	Drits et al. (1997)
Dioct.	Glauconite	Kul-2	0		3.72	0.28	0.00	0.84	0.40	0.55	0.26	nr	nr	2.05	0.81	1.21	0.00	0.02	0.00	0.77		Zaitseva et al. (2008)
Dioct.	G-N	Glauconite Bsh-11	<10		3.69	0.31	0.00	1.04	0.42	0.38	0.22	nr	nr	2.06	0.60	1.02	0.00	0.02	0.00	0.74		Zaitseva et al. (2008)
Dioct.	G-N	Glauconite Dobre	5		3.64	0.36	0.00	0.76	0.31	0.79	0.15	nr	nr	2.01	0.94	1.25	0.00	0.04	0.01	0.70		Kotlicki et al. (1981)
Dioct.	G-N	Glauconite K4	15		3.83	0.17	0.00	0.59	0.45	0.86	0.09	nr	nr	1.99	0.95	1.40	0.00	0.05	0.00	0.63		Kotlicki et al. (1981)
Dioct.	Glauconite	Pil	0		3.75	0.27	0.00	0.44	0.42	0.93	0.21	nr	nr	2.00	1.14	1.56	0.00	0.05	0.06	0.75	1.513	Drits et al. (1997)
Dioct.	Glauconite	655	0		3.71	0.24	0.00	0.16	0.63	1.10	0.12	nr	nr	2.01	1.22	1.85	0.00	0.05	0	0.92	1.515	Drits et al. (1997)
Dioct.	G-N	Va22-146KS (1144-1145)	68		3.93	0.05	0.02	0.00	0.25	1.69	0.05	0.00	0.00	2.00	1.76	2.01	0.00	0.00	0.12	0.25	1.510	Cuadros et al. (2013)
Dioct.	G-N	Va22-146KS (1030-1034)	23		3.80	0.02	0.18	0.06	0.17	1.58	0.11	0.05	0.00	1.98	1.87	2.04	0.00	0.04	0.03	0.49	1.511	Cuadros et al. (2013)
Dioct.	G-N	Va22-146KS (603-604)	50		3.74	0.04	0.22	0.03	0.18	1.79	0.00	0.00	0.00	2.00	2.01	2.19	0.00	0.06	0.00	0.33	1.515	Cuadros et al. (2013)
Dioct.	G-N	Va22-146KS (612-614)	59		3.68	0.09	0.23	0.02	0.20	1.79	0.00	0.00	0.00	2.02	2.02	2.22	0.00	0.09	0.00	0.27	1.514	Cuadros et al. (2013)
Dioct.	G-N	Va22-146KS (588-591)	56		3.73	0.00	0.27	0.05	0.17	1.73	0.04	0.00	0.00	1.99	2.04	2.21	0.00	0.09	0.00	0.35	1.512	Cuadros et al. (2013)
Dioct.	G-N	Va22-146KS (586-587)	39		3.55	0.09	0.36	0.02	0.18	1.83	0.04	0.00	0.00	2.08	2.23	2.41	0.00	0.07	0.00	0.30	1.514	Cuadros et al. (2013)
Dioct.	G-N	Va22-146KS (639-640)	33		3.62	0.00	0.38	0.00	0.23	1.84	0.00	0.00	0.00	2.08	2.22	2.45	0.00	0.05	0.00	0.28	1.511	Cuadros et al. (2013)
Di.-Tri.	T-N	Va22-146KS (583-586)	69		3.42	0.21	0.37	0.05	0.18	1.96	0.00	0.00	0.01	2.21	2.33	2.51	0.00	0.00	0.01	0.13	1.516/1.532	Cuadros et al. (2013)
Di.-Tri.	T-N	Va22-146KS (602-603)	60		3.13	0.45	0.42	0.00	0.28	1.97	0.00	0.01	0.01	2.27	2.39	2.67	0.00	0.09	0.03	0.11	1.515/1.533	Cuadros et al. (2013)
Di.-Tri.	T-N	Va22-146KS (575-577)	71		3.40	0.10	0.50	0.03	0.18	1.92	0.00	0.00	0.00	2.13	2.42	2.60	0.00	0.12	0.00	0.15	1.515/1.534	Cuadros et al. (2013)
Di.-Tri.	T-N	CHN-100-18PC (290-292)	68		3.13	0.37	0.50	0.00	0.18	1.81	0.20	0.08	0.01	2.28	2.51	2.69	0.00	0.19	0.00	0.09	1.513/1.530	Cuadros et al. (2013)
Di.-Tri.	T-N	Va22-146KS (471-475)	75		3.24	0.14	0.62	0.14	0.15	1.69	0.20	0.01	0.01	2.21	2.51	2.66	0.00	0.10	0.09	0.21	1.514/1.533	Cuadros et al. (2013)
Di.-Tri.	T-N	Va3-413KH (150-153)	80		3.11	0.23	0.66	0.00	0.55	1.68	0.07	0.02	0.00	2.33	2.41	2.96	0.00	0.13	0.16	0.13	1.536	Cuadros et al. (2013)
Trioct.	Fe-saponite	Synthetic MF9		100	4.00	0.00	0.00	0.00	2.43	0.30	0.00	0.00	0.00	2.73	0.30	2.73	0.00	0.00	0.26	0.00	1.525[a]	Grauby et al. (1994)
Trioct.	Fe-saponite	Fe-saponite		100	3.56	0.44	0.00	0.02	2.35	0.00	0.58	0.00	0.00	2.95	0.58	2.93	0.00	0.12	0.30	0.00	1.526	Andrews et al. (1983)
Trioct.	Fe-talc			0	3.98	0.01	0.00	0.01	2.98	0.01	0.02	0.00	0.00	3.01	0.03	3.01	0.00	0.00	0.00	0.00		Martin et al. (1999)
Trioct.	T-S	M64/1 139GTV-5E (Turtle Pits)		21	3.78	0.19	0.03	0.00	2.80	0.03	0.20	0.00	0.00	3.03	0.26	3.06	0.00	0.00	0.13	0.00	1.530	Cuadros et al. (2013)
Trioct.	Fe-saponite	Synthetic MF8		100	3.96	0.00	0.04	0.00	2.03	0.56	0.00	0.00	0.00	2.59	0.60	2.63	0.00	0.00	0.32	0.00	1.524[a]	Grauby et al. (1994)
Trioct.	Fe-saponite	Synthetic N5		100	3.93	0.00	0.07	0.00	2.30	0.03	0.43	0.00	0.00	2.76	0.53	2.83	0.00	0.00	0.50	0.03	1.535[a]	Baldermann et al. (2014)

Trioct.	T-S	Sea Cliff Dive 308		27	3.86	0.05	0.09	0.06	2.58	0.05	0.29	0.00	0.00	2.99	0.43	3.01	0.00	0.01	0.02	0.01	1.524	Cuadros et al. (2013)
Trioct.	T-S	Va3-413KH (313-318)		18	3.76	0.06	0.18	0.00	2.51	0.24	0.20	0.00	0.00	2.94	0.62	3.13	0.00	0.05	0.00	0.00	1.530	Cuadros et al. (2013)
Trioct.	Fe-saponite	Synthetic N8		100	3.82	0.00	0.18	0.00	1.54	0.07	1.17	0.00	0.00	2.78	1.42	2.96	0.00	0.00	0.52	0	1.542[a]	Baldermann et al. (2014)
Trioct.	T-S	Va3-413KH (382-389)		90	3.59	0.21	0.20	0.00	2.03	0.51	0.18	0.00	0.01	2.73	0.89	2.92	0.00	0.06	0.31	0.00	1.533	Cuadros et al. (2013)
Trioct.	Fe-saponite	Synthetic N14		100	3.74	0.00	0.26	0.00	0.31	0.18	2.27	0.00	0.00	2.76	2.71	3.02	0.00	0.00	0.53	0.01	1.544[a]	Baldermann et al. (2014)
Trioct.	T-S	1183-9		2	3.57	0.04	0.39	0.00	1.52	0.75	0.55	0.01	0.00	2.83	1.69	3.21	0.00	0.01	0.00	0.00	1.53	Cuadros et al. (2013)
Trioct.	Biotite	MT-1		0	2.73	1.27	0.00	0.20	1.25	0.33	0.89	0.05	0.09	2.82	1.22	2.47	0.00	0.05	0.04	0.80		Dyar & Burns (1986)
Trioct.	Biotite	SL-18		0	2.75	1.25	0.00	0.12	1.06	0.29	1.08	0.02	0.16	2.72	1.37	2.43	0.00	0.04	0.04	0.96		Dyar & Burns (1986)
Trioct.	Biotite	BP-1		0	2.80	1.20	0.00	0.17	1.36	0.31	0.83	0.03	0.10	2.79	1.14	2.50	0.00	0.05	0.03	0.81		Dyar & Burns (1986)
Trioct.	Biotite	MG-1		0	2.74	1.26	0.00	0.09	1.31	0.32	0.92	0.03	0.14	2.81	1.24	2.55	0.00	0.05	0.03	0.81		Dyar & Burns (1986)
Trioct.	Biotite	BF 9A		0	2.60	1.40	0.00	0.32	1.09	0.13	1.19	0.01	0.15	2.89	1.32	2.41	0.00	0.00	0.06	0.82		Dyar & Burns (1986)
Trioct.	Biotite	BF 9E		0	2.64	1.36	0.00	0.41	1.07	0.19	1.15	0.00	0.08	2.89	1.34	2.41	0.00	0.00	0.05	0.78		Dyar & Burns (1986)
Trioct.	Biotite	BF 9G		0	2.68	1.32	0.00	0.40	1.07	0.13	1.18	0.00	0.08	2.87	1.31	2.39	0.00	0.00	0.04	0.85		Dyar & Burns (1986)
Trioct.	Ferriphlogopite	Tpq 16-4Aa		0	2.91	0.71	0.38	0.00	2.64	0.1	0.22	0.01	0.03	3.00	0.70	3.34	0.00	0.00	0.00	0.99	1.541	Brigatti et al. (1999)
Trioct.	Ferriphlogopite			0	2.97	0.64	0.39	0.15	2.55	0.00	0.24	0.00	0.01	2.95	0.62	3.18	0.00	0.00	0.01	0.95		Dyar & Burns (1986)
Trioct.	Ferriphlogopite	Tpq 16-4Ac		0	3.01	0.13	0.86	0.00	1.99	0.30	0.54	0.02	0.01	2.86	1.70	3.69	0.00	0.00	0.01	0.99	1.551	Brigatti et al. (1999)
Trioct.	Ferriphlogopite	Tas 22-1b		0	3.07	0.00	0.93	0.00	2.75	0.06	0.17	0.01	0.01	3.00	1.16	3.91	0.00	0.00	0.02	0.98	1.546	Brigatti et al. (1999)
Trioct.	Annite	865DS		0	2.75	1.25	0.00	0.01	0.12	0.28	2.08	0.04	0.22	2.75	2.36	2.48	0.00	0.04	0.08	0.88		Dyar & Burns (1986)
Trioct.	Ferriannite	GE		0	3.03	0.54	0.43	0.00	1.35	0.15	1.48	0.00	0.00	2.98	2.05	3.40	0.00	0.00	0.02	0.83		Dyar & Burns (1986)
Trioct.	Ferriannite	BHD2/448		0	2.92	0.52	0.55	0.00	0.38	0.12	2.38	0.00	0.01	2.90	3.06	3.44	0.00	0.06	0.00	1.03		Dyar & Burns (1986)

nr: Not reported.

nd: Not determined.

[a] Assessed from plots in the article.

Most T-N samples have two 060 peaks, corresponding to dioctahedral and trioctahedral domains.

This is a preprint, the final version is subject to change, of the American Mineralogist (MSA)
Cite as Authors (Year) Title. American Mineralogist, in press.
DOI: https://doi.org/10.2138/am-2019-7036

Table 2. Mössbauer parameters for spectra in Figure 3.

	Sample	Cy 82-14-5	Va22..586-587	Va22..575-577	Va3..382-389
	Mineralogy	N	G-N	T-N	T-S
	Velocity scale (mm/s)	+/- 4	+/- 4	+/- 4	+/- 4
Tet Fe(III)	IS (mm/s)	0.14	0.12	0.15	0.13
	QS (mm/s)	0.65	0.45	0.66	0.88
	Width (mm/s)	0.38	0.26	0.40	0.46
	Area (%)	17	13	21	30
Oct Fe(III)	IS (mm/s)	0.38	0.41	0.41	
	QS (mm/s)	0.54	0.42	0.42	
	Width (mm/s)	0.51	0.45	0.47	
	Area (%)	67	67	61	
Oct Fe(III)	IS (mm/s)	0.46	0.46	0.45	0.54
	QS (mm/s)	0.89	0.85	0.85	1.06
	Width (mm/s)	0.46	0.31	0.32	0.44
	Area (%)	16	18	18	31
Oct Fe(II)	IS (mm/s)		1.05		1.13
	QS (mm/s)		2.04		2.66
	Width (mm/s)		0.23*		0.36
	Area (%)		2		15
Hematite (Oct Fe[III])	IS (mm/s)				0.34
	QS (mm/s)				1.00
	Width (mm/s)				0.36
	Area (%)				25
	χ^2	450.1	315.7	377.5	375.2
	χ^2_{norm}	0.9	0.6	0.7	0.7

*Parameter fixed in the curve-fitting process.

IS = isomer shift.

QS = quadrupole splitting.

Width = full width at half maximum.

Area is expressed as percentage of the total peak area.

χ^2 = Goodness of fit.

χ^2_{norm} = Goodness of fit normalized to number of data points.

This is a preprint, the final version is subject to change, of the American Mineralogist (MSA)
Cite as Authors (Year) Title. American Mineralogist, in press.
DOI: https://doi.org/10.2138/am-2019-7036

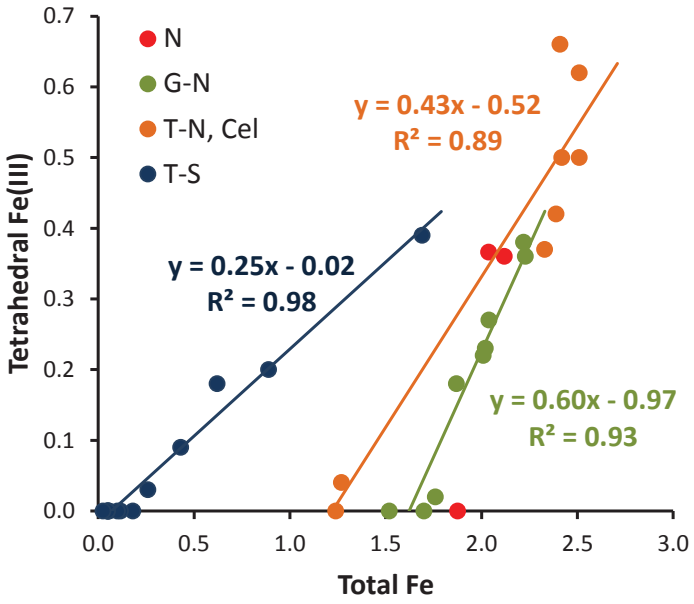

Fig. 1

This is a preprint, the final version is subject to change, of the American Mineralogist (MSA)
Cite as Authors (Year) Title. American Mineralogist, in press.
DOI: https://doi.org/10.2138/am-2019-7036

Fig. 2

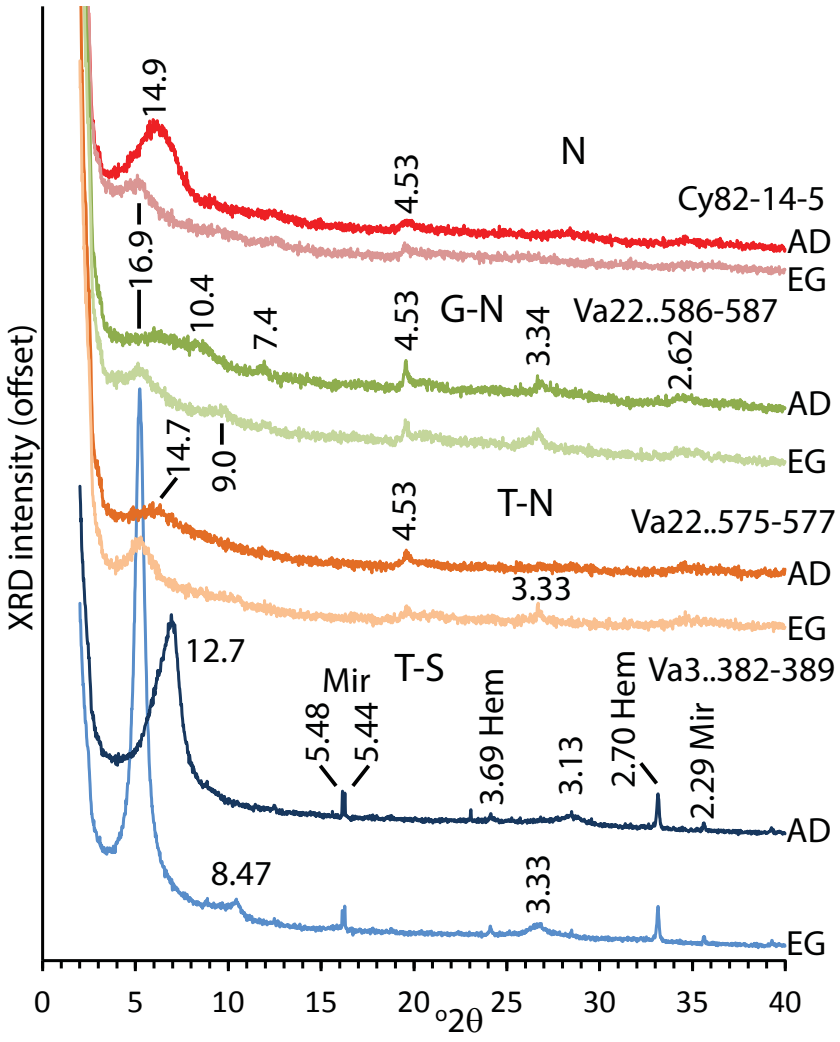

This is a preprint, the final version is subject to change, of the American Mineralogist (MSA)
Cite as Authors (Year) Title. American Mineralogist, in press.
DOI: https://doi.org/10.2138/am-2019-7036

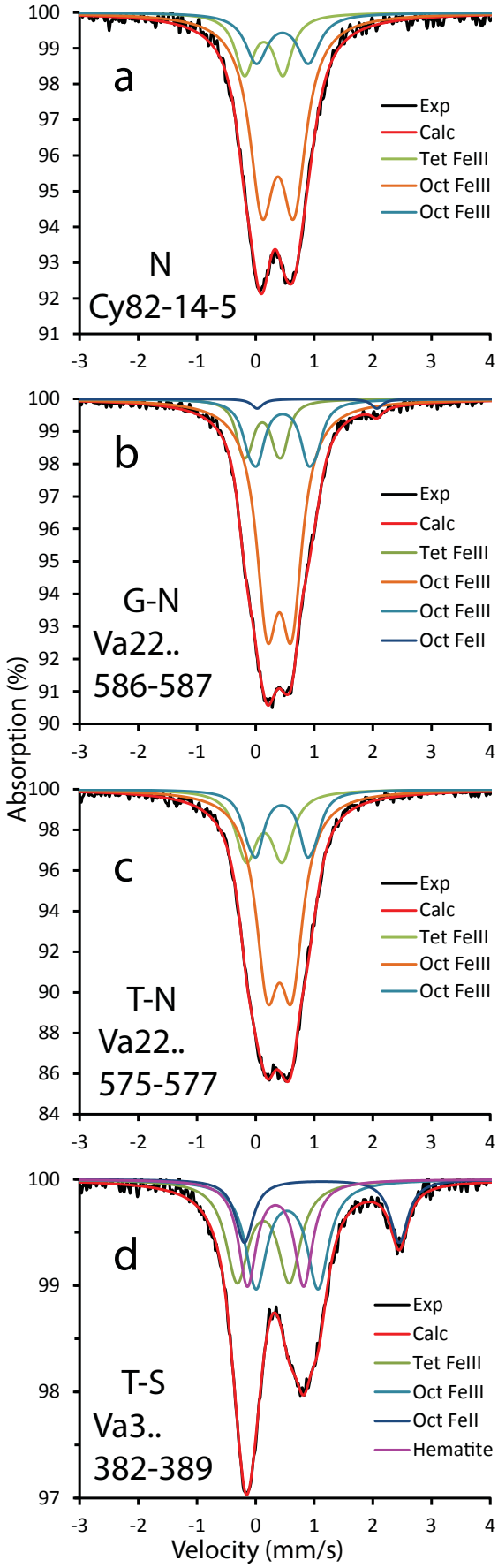

Fig. 3

This is a preprint, the final version is subject to change, of the American Mineralogist (MSA)
Cite as Authors (Year) Title. American Mineralogist, in press.
DOI: https://doi.org/10.2138/am-2019-7036

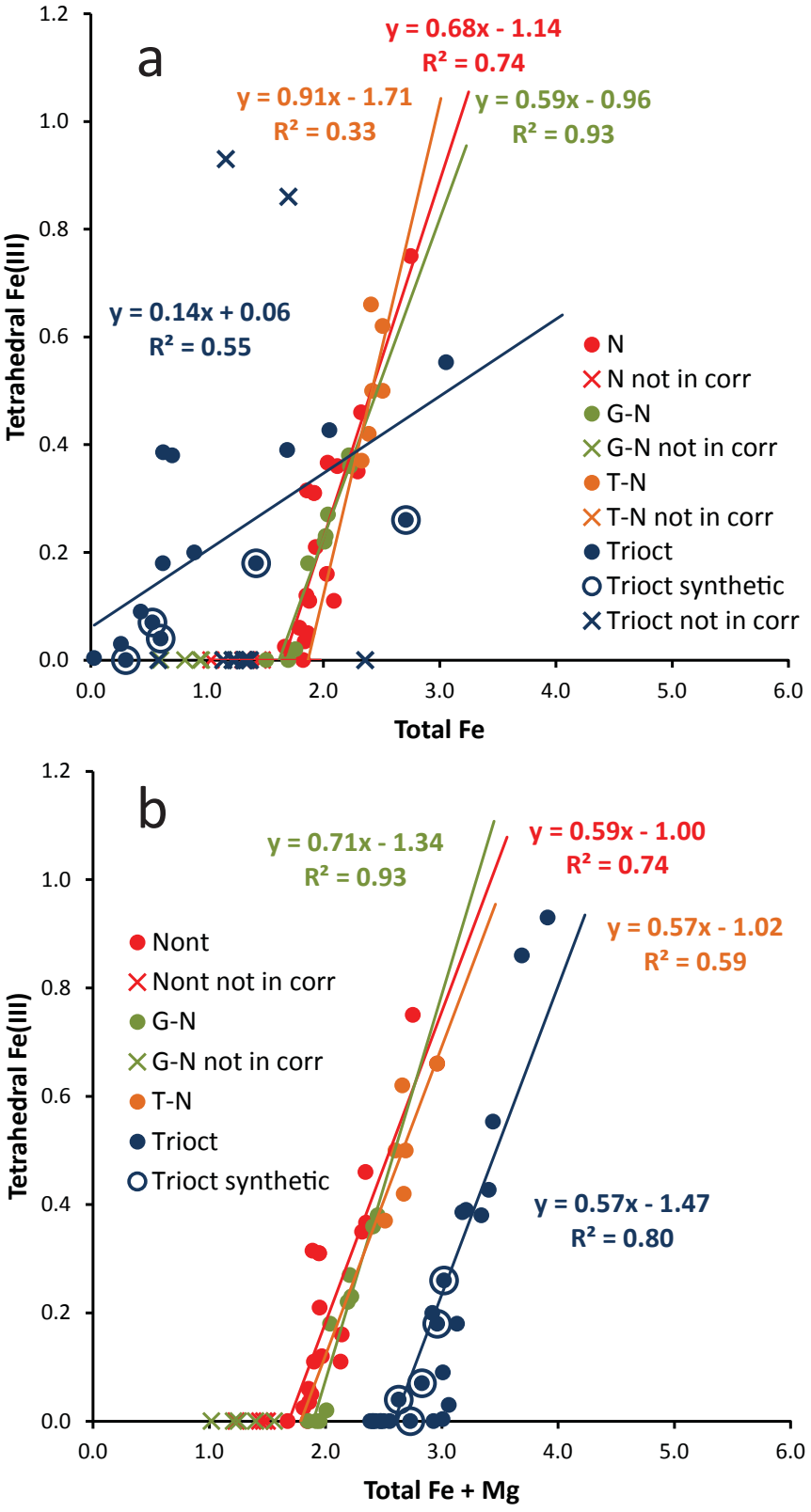

Fig. 4

This is a preprint, the final version is subject to change, of the American Mineralogist (MSA)
Cite as Authors (Year) Title. American Mineralogist, in press.
DOI: https://doi.org/10.2138/am-2019-7036

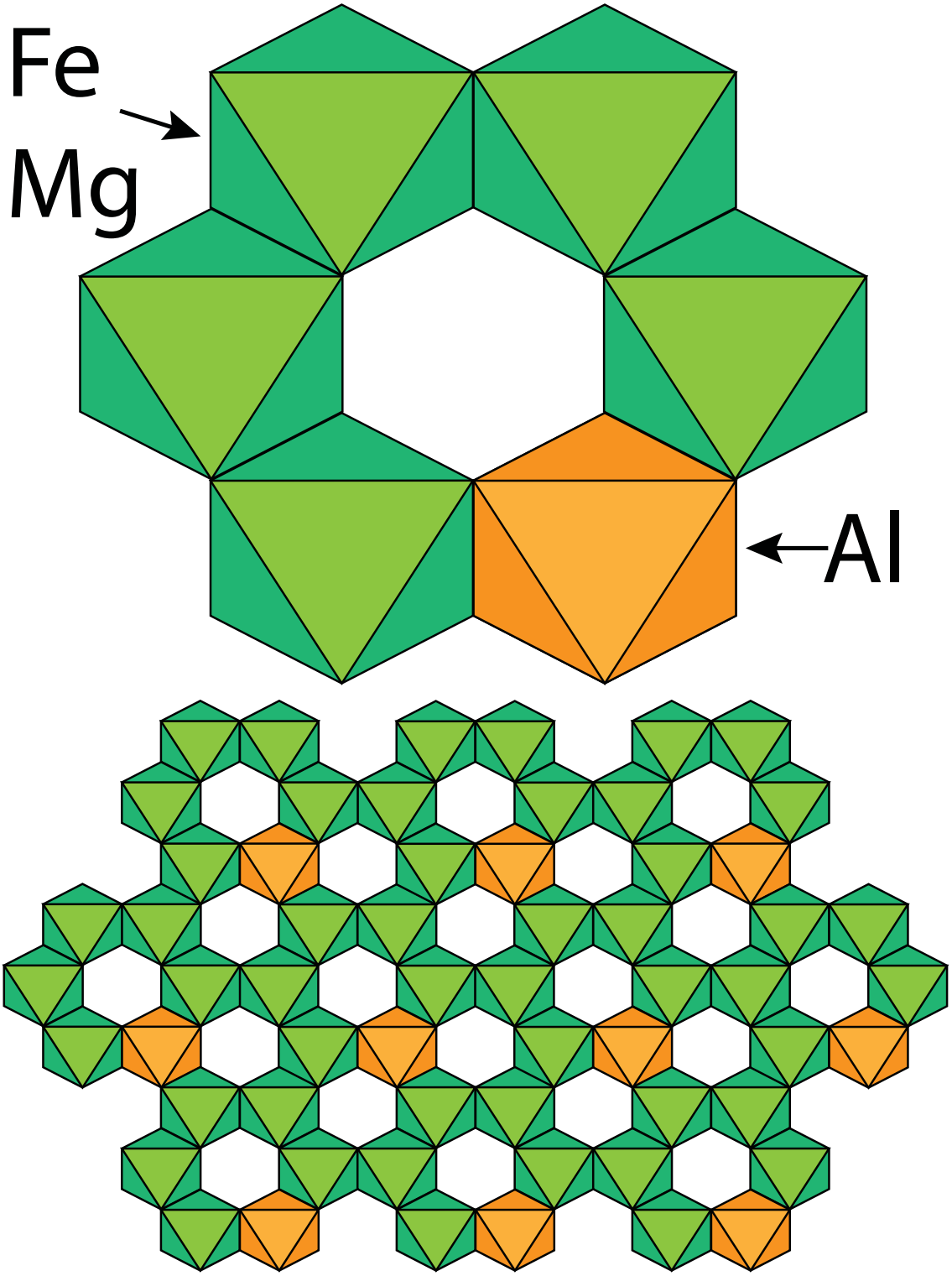

This is a preprint, the final version is subject to change, of the American Mineralogist (MSA)
Cite as Authors (Year) Title. American Mineralogist, in press.
DOI: https://doi.org/10.2138/am-2019-7036

Fig. 6

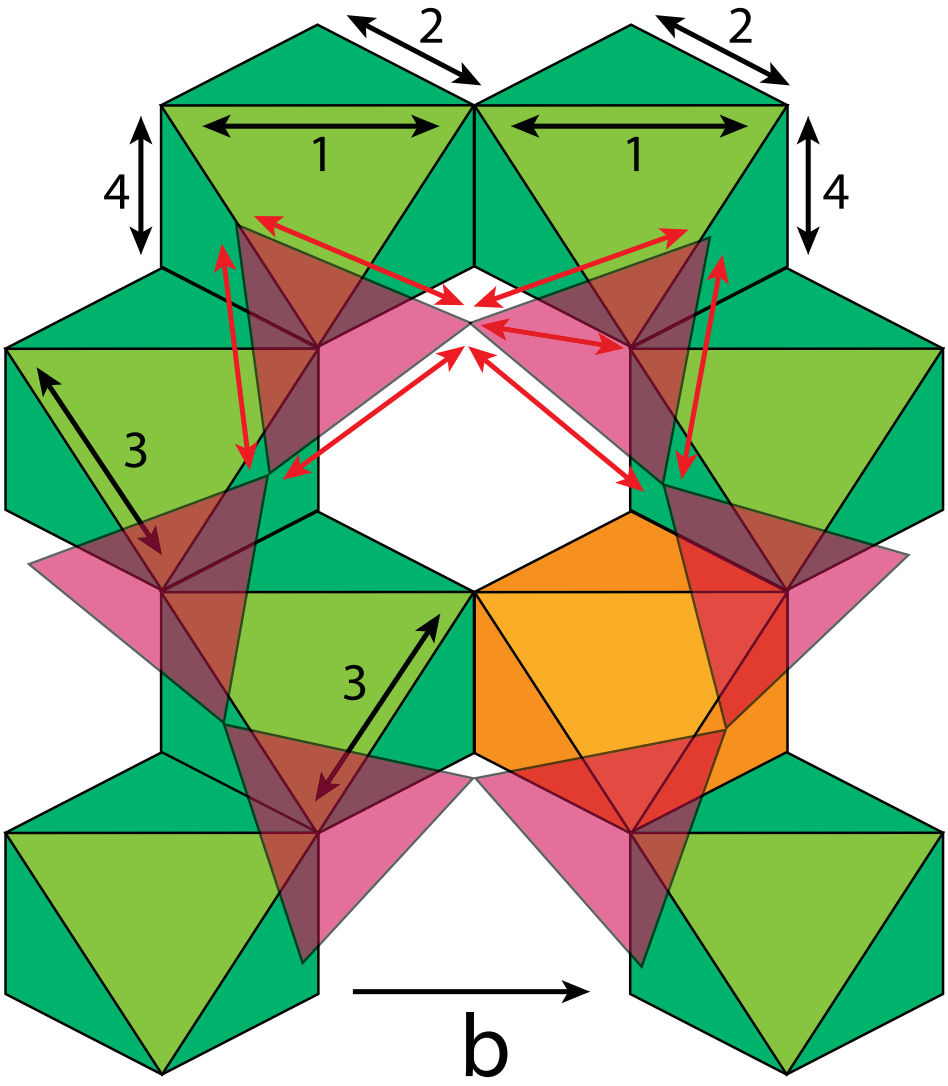

This is a preprint, the final version is subject to change, of the American Mineralogist (MSA)
Cite as Authors (Year) Title. American Mineralogist, in press.
DOI: https://doi.org/10.2138/am-2019-7036

Fig. 7

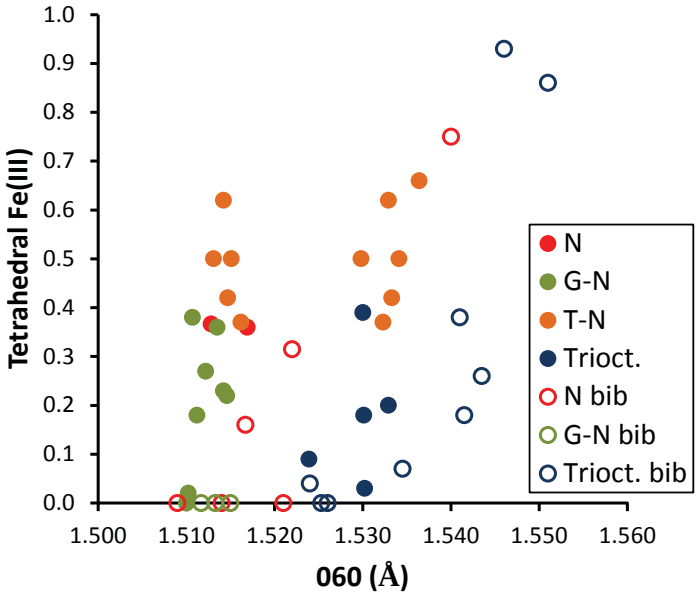

This is a preprint, the final version is subject to change, of the American Mineralogist (MSA)
Cite as Authors (Year) Title. American Mineralogist, in press.
DOI: https://doi.org/10.2138/am-2019-7036

Fig. 8